Numerical modelling and experimental investigation of the Riv-Bonding process

Yunpeng Liu[a], Li Han[b], Huan Zhao[a] and Xianping Liu[a,*]

[a] School of Engineering, University of Warwick, Coventry CV4 7AL, UK

[b] Hansher Consulting Ltd., Coventry, UK

* X.Liu@warwick.ac.uk

Abstract:

Nowadays, the Riv(et)-Bonding technique has become a major joining approach in the automotive industry. It effectively incorporates the benefits of the adhesive bonding and the self-pierce riveting (SPR), but overcomes their individual drawbacks. Finite element (FE) simulation of the SPR process now plays a very important role during the product design and manufacture processes in the automotive field. However, there is no reported progress in the simulation of the Riv-Bonding process. To deepen understandings of this joining method, a FE model of the Riv-Bonding process suitable for industrial applications was developed in this study. The Ostwald-de Waele power law was adopted to approximately represent properties of the adhesive SikaPower 498. Interrupted laboratory tests of the SPR process and the Riv-Bonding process were carried out to calibrate the FE model, and another eight types of joints were experimentally made to verify the effectiveness of the developed model. Meanwhile, the effects of the adhesive layer on the joint quality and the riveting process were analysed by comparing the interrupted test results of the two processes. The adhesive distribution during the Riv-Bonding process was also discussed. The developed model was proven capable of predicting the Riv-Bonding process, including the adhesive distribution, the solid parts deformation and the load-displacement curve. Unlike the SPR simulation, the blank-holder strike during the clamping stage should be properly modelled in the simulation model of the Riv-Bonding process, due to its noticeable influences on the adhesive distribution as well as on the top sheet deformation. It was also found that, under the studied joint configuration, the adhesive layer demonstrated slightly negative effects on the riveted connection of the Riv-Bonded joints. The simulation model developed in this study lays a foundation for further quality prediction and mechanical strengths modelling of the Riv-Bonded joints.

Keywords: Riv-Bonding process; SPR process; FE; Adhesive distribution; Interrupted test; Rate power law

1 Introduction

In the automotive industry, the Riv(et)-Bonding technique has been widely adapted for the assembly of aluminium Body in White (BIW). It simply combines the adhesive bonding and the self-pierce riveting (SPR) together to achieve a more reliable and efficient connection. Sun et al. (2007) found that the adhesive layer in the Riv-Bonded joint could effectively reduce the stress concentration around the riveted zone, and avoid the galvanic corrosion caused by direct contacts between dissimilar metals. Most importantly by involving an adhesive layer, the riveted structure's noise, vibration and harshness (NVH) performance could be dramatically improved. Unlike the adhesive bonded structure, the riveted connection is less sensitive to the service environments. Di Franco and Zuccarello (2014) revealed that the riveted connection could effectively overcome the mechanical strength decay of the adhesive bonded connection when exposed in the environments with high moisture, high temperature or corrosive agents. Such advantages have also been adapted by other relatively new joining processes, like Weld-Bonding, Bolt-Bonding and Clinch-Bonding. It has been proved in many studies that the joints made with these joining techniques could achieve a better performance than pure mechanical or thermal connected joints. For example, Balawender et al. (2011) found that the Clinch-Bonded joint had a much higher lap shear strength than the clinched joint. Esmaeili et al. (2015) discovered that the Bolt-Bonded joint had a higher fatigue life compared with the pure bolted joint. Therefore, these joining methods have also been widely used in the industrial field.

Take two sheets connection as an example, **Fig. 1** schematically shows the adhesive bonding process, the SPR process and the Riv-Bonding process. As presented in **Fig. 1**(a), the adhesive is applied on the bottom sheet, and then the top sheet is placed over the adhesive bead. A pressure is applied on the top sheet to make the adhesive distributed uniformly between the two sheets. Different methods can be used to control the thickness of the adhesive layer. For instance, Weidong Dang (2015) added glass balls with a specific diameter into the adhesive to control the adhesive thickness, while spacers with specific thicknesses were adopted in the study of Da Silva et al. (2006). For the SPR process in **Fig. 1**(b), the two sheets are clamped together by the blank-holder, then the punch moves downwards and presses the rivet into the two sheets. The two parts are finally connected by a mechanical interlock formed between the bottom sheet and the rivet shank. During the Riv-Bonding process, as shown in **Fig. 1**(c), the adhesive is applied on the bottom sheet and distributed between the two sheets after the clamping process. Then, the normal SPR process is carried out to form the Riv-Bonded connection. Different from the adhesive bonding, the adhesive thickness of the Riv-Bonded joint is controlled roughly by the applied amount of the adhesive or the interval time between the clamping stage and the riveting process.

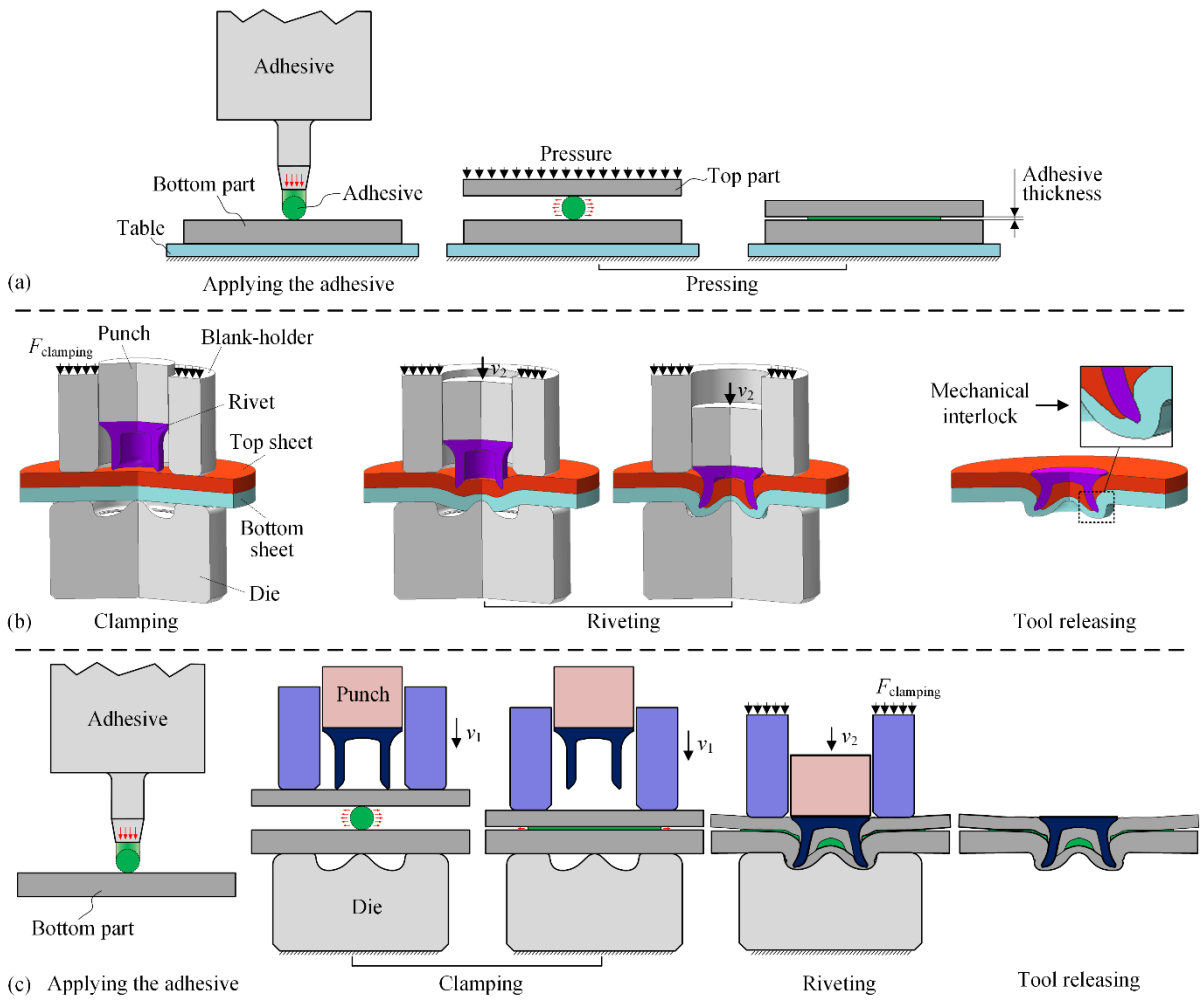

Fig. 1 Schematics of the (a) Adhesive bonding process, (b) Self-piercing riveting process and (c) Riv-Bonding process

Adhesive bonding, as one frequently used connecting method, has been extensively studied by many researchers. Most of the studies focused on the mechanical performance evaluation and prediction of the adhesive bonded joints. For example, Alfano et al. (2011) revealed that the shear strength of the adhesive bonded joint could be improved by laser surface treatments, but the amount of the improvement depended heavily on the adhesive property. Ozenc and Sekercioglu (2014) found that the shear strength of the adhesive bonded joint showed a decreasing trend with the increment of the service temperature. Arenas Ã et al. (2009) evaluated the influence of adhesive thickness on the shear strength of the adhesive bonded joint, and discovered that the joint shear strength increased when the adhesive thickness decreased from 0.8mm to 0.4mm under the studied experimental conditions. Except for experimental tests, a considerable number of simulation models have been developed to study the stress distribution as well as the crack propagation within the adhesive layer, and to predict the shear and tensile strength of the adhesive bonded joints. Two methods are frequently adopted to simulate the adhesive bonded joints. The first one is to use traditional continuum elements to model the adhesive layer. This allows predictions of the stress distribution, the adhesive thickness effect and the plastic behaviour

of the cured adhesive. However, this method could not model the adhesive failure and is sensitive to the mesh size. Whilst the second method is to use interface elements (finite thickness or zero thickness) in conjunction with traction-separation laws to model the adhesive layer. This method was adopted by Anyfantis and Tsouvalis (2012) to simulate the lap-shear tests of the adhesive bonded joints. The simulation results showed a good agreement with the experimental results in terms of the load-displacement and load-strains curves. With the cohesive zone modelling (CZM) technique, this method can effectively avoid the stress singularity around the edges of the cured adhesive layer. It is also convenient to be implemented in Finite Element (FE) software and relatively insensitive to the mesh size. The drawbacks of this method are that the fracture position should be predefined empirically, and the shape of the traction-separation law should be properly selected. In addition to the two methods, Santos and Campilho (2017) also demonstrated the capability of the eXtended Finite Element Method (XFEM) for modelling of the adhesive bonded joint. Studies relating to the FE analysis of the adhesive bonded joint were comprehensively reviewed and discussed by He (2011) and Sauer (2016).

Self-pierce riveting (SPR) has also been widely investigated: from its joining process to the mechanical performances of the SPR joints. For example, Haque et al. (2012) found that the load-displacement curve, in addition to process monitoring, could be also used to identify the events happened during the SPR process, such as the top sheet separation and the start of the rivet flaring into the bottom sheet. The performances of the SPR technique for different sheet materials, sheet thickness combinations and layers of stack have been widely studied. Fratini et al. (2009) found that the SPR can be effectively used to join fiberglass composite sheet with aluminium alloy AA6082-T6 sheet if the composite sheet was used as the top sheet. Abe et al. (2008) experimentally studied the performance of the SPR method for three-layer sheets. The aluminium alloy AA5052-H34 sheet was fixed as the bottom layer, while the materials for the top and middle layers were chosen from five types of high strength steels and AA5052-H34. It was found that the interlock showed a decrease tendency when the strength of the top or middle sheet increased. A better joint quality can be obtained if the hardest sheet was used as the middle layer. To facilitate the joint quality optimization, the influences of SPR process parameters, such as the die profile, the rivet materials and the rivet profile, on the critical joint quality indicators have been investigated. Ma et al. (2018) studied the influence of the die diameter and pip height on the quality of the SPR joints with AA6061-T6 and mild steel CR4 sheets. It was found that the variation of the die diameter and pip height could apparently affect the joint quality by changing the deformation behaviours of the rivet and sheets. Van Hall et al. (2018) explored the effects of the rivet surface decarburization on the rivet column strength and ability to flare during the SPR process. It was found that the intentional surface decarburization of the rivet can prevent the formation of fractures along the rivet leg periphery, while maintaining a sufficient column strength to pierce through the sheet without buckling of the rivet shank. The mechanical performances of the SPR joints, such as shear strength, T-peel strength, fatigue life and energy absorption,

have also been intensively evaluated. Zhang et al. (2020) studied the fatigue characterization and failure modes of the SPR joints with titanium sheets. The experimental results revealed that the crack propagation mechanisms and fretting behaviours vary with the different joint failure modes. In addition to experimental investigations, numerous simulation models of the SPR process have been developed to study the joining process and to predict the joint quality under different joint configurations. Porcaro et al. (2006) developed a 2D simulation model of the SPR joints with AA6060 sheets in LS-DYNA. Under the studied sixteen joint configurations, the predicted load-displacement curve as well as the deformations of the rivet and sheets showed good agreements with the experimental results. Qu and Deng (2008) proposed a 2D simulation model of SPR joints with Al6061 sheets in MSC.SuperForm. The strain rate hardening effect and the temperature softening effect on the sheet material were considered using the Johnson and Cook material model. Ishikawa and Aihara (2017) explored the performances of the Arbitrary Lagrangian–Eulerian (ALE), the Coupled Eulerian-Lagrangian (CEL) and the Smoothed-Particle Hydrodynamics (SPH) modelling techniques on the SPR simulation. Simulation models were also developed to predict the mechanical strengths of the SPR joints. Hoang et al. (2011) studied the effects of the natural aging, pre-strain and history data during SPR process on the static strengths of SPR joints using a 3D FE model in LS-DYNA. Moraes et al. (2019) numerically studied the effects of the residual stress and strain hardening on the shear strength of SPR joints using a 3D simulation model in ABAQUS. Huang et al. (2017) established a 3D simulation model using ABAQUS to study the fatigue behaviour of the SPR joints with aluminium alloy 6111-T4 sheets. A reasonable agreement was found in predictions on crack initiation site, final crack aspect ratio and fatigue life when comparing the simulation and experimental results. Hönsch et al. (2020) proposed a 3D simulation model to predict the failure modes and the mechanical strengths of SPR joints with 6xxx aluminium alloy sheets under different loading conditions. The numerical and experimental studies relating to the SPR technique have been systematically reviewed by He et al. (2012) and Li et al. (2017).

Although the Riv-Bonding has been broadly used in the automotive industry, only very limited studies can be found in the public domain. Almost all of them focused on the mechanical performance in comparison between Riv-Bonded joints and SPR joints. For instance, the shear strength of the Riv-Bonded joints with a hot-melt adhesive was studied by Baurova et al. (2017). The experiment results revealed that the Riv-Bonded joints had an apparently higher shear strength than the SPR joints. He et al. (2013) studied the shear strength and energy absorption of the Riv-Bonded joints made with AA5754 sheets and a 0.1mm adhesive layer. The experiment results indicated that the Riv-Bonded joint had a 14% higher maximum shearing load, but a much lower energy absorption than that of the solo SPR joint. Liu and Zhuang (2019) experimentally studied the shear strength and failure modes of the Riv-Bonded joints with the top sheet of carbon fibre reinforced polymer (CFRP) and AA5754-H22 as the bottom sheet. It was found that the ply angle of the CFRP and the

sheet thickness had significant impacts on the shear strength and failure modes of the Riv-Bonded joints. Sun et al. (2007) found that the involved adhesive layer (Dow Betamate 4601) apparently improved the fatigue performance of the SPR joints under the lap-shearing loading, but a smaller improvement was observed under the cross-tension loading. Miyashita et al. (2011) investigated the shear strength and fatigue strength of the Riv-Bonded joints with AM50 magnesium alloy sheets. The test results indicated that the adhesive layer could not eliminate the cracks on the bottom sheet, but effectively improve the joint shear strength and fatigue strength. It was also found that the adhesive properties had significant influence on the shear strength of the Riv-Bonded joints. Similarly, Guo and El-Tawil (2020) also experimentally evaluated the influences of the sheet material properties and the adhesive layer on the joint shear strength and fatigue performance.

These studies on the performances of the Riv-Bonded joints have undoubtedly helped the applications of this joining approach in the industrial field. However, in the digital manufacturing era, a suitable simulation tool is even more desirable in order to better understand the Riv-Bonding process, and to facilitate the joint quality optimization. So far, the only accessible simulation model of the Riv-Bonding process was reported by Fricke and Vallée (2016). In their study, two simulation software were used: one for the modelling of solid parts using structural finite element method (FEM), and another for the modelling of the uncured adhesive (a high viscosity fluid) using computational fluid dynamic (CFD) method. In addition, a coupling software was also used to exchange information at the fluid-structure interfaces between the two software. The reason of using three software was triggered by the different natures between the solid and fluid. The results indicated a reasonable agreement between the simulation and the experimental tests. However, despite the long time to set up the simulation model, this co-simulation method is also computationally expensive and requires a wide knowledge on three different software. In the fast-growing digital automotive industry, an easy-to-use and fast response simulation model of the Riv-Bonding process is urgently needed.

The biggest challenge for the Riv-Bonding simulation is how to model the fluid-structure interaction (FSI) between the uncured adhesive and other solid parts. A promising solution is the Ostwald–de Waele power law, which approximately describes the fluid flow behaviour by establishing a relationship between the shear stress and shear rate of the fluid. Due to the simplicity, it has already been adopted in many studies to model the fluid flow behaviour. For example, Andersson et al. (1996) mathematically investigated the flow of thin liquid film caused by an unsteady stretched surface. The impact of fluid types on the velocity profile within the thin liquid film was studied by changing the power-law index of the Ostwald-de Waele power law. Jabbari et al. (2013) predicted the wet tap thickness and velocity distribution inside the slurry flow using a proposed mathematical model. The Ostwald-de Waele power law combined with a simple quasi-steady momentum equation were employed to describe the flow behaviour of the slurry containing material. The predicted

results matched well with the results from rheological experiments. Recently, based on the simulation method proposed by Ardakani (2012), Gerstmann and Awiszus (2020) successfully developed a fast response simulation model of the Clinch-Bonding process. Both of the solid components and the uncured adhesive were modelled using the structural FE method. The Ostwald-de Waele power law was used to model the uncured adhesive and showed a very good performance. Therefore, the Ostwald-de Waele power law is a promising constitutive model for the uncured adhesive in the simulation of the Riv-Bonding process.

The objective of this research is to develop a fast response and easy-to-use simulation model of the Riv-Bonding process. Commercial software Simufact.Forming, which has been widely adopted in the automotive industry, was selected. All the solid parts (i.e. the rivet and sheets) and the uncured adhesive layer were modelled using traditional lagrangian elements. The Ostwald–de Waele power law was adopted to model the adhesive (SikaPower 498) flow during the Riv-Bonding process. Interrupted laboratory tests of the Riv-Bonding process and the SPR process were performed to calibrate the simulation model, and further eight types of joints (four SPR joints and four Riv-bonded joints) were experimentally made to verify the performance of the developed model. The impacts of the adhesive layer on the riveting process and on the joint quality were also experimentally analysed. This study provides a better understanding of the Riv-Bonding process and lays a foundation for further quality prediction and mechanical strengths modelling of the Riv-Bonded joints.

2 Experiment tests

To establish the simulation model of the Riv-Bonding process, experimental tests were performed to collect necessary data for the model calibration and verification.

2.1 Sample preparation

Boron steel rivets with hardness 280±30HV10 and aluminium alloy AA5754 sheets were used throughout the experiment. The structural adhesive SikaPower 498 was selected and its basic properties are listed in **Table 1**. This is a one component epoxy resin-based adhesive and can achieve a high mechanical strength once cured. This adhesive can be applied on oiled or coated surfaces, and suitable for connections with other joining methods (e.g., resistance spot welding, SPR and clinching) (*SikaPower*®-498, 2016). To calibrate the simulation model and to study the impacts of the adhesive layer on the Riv-Bonding process, interrupted laboratory tests of the Riv-Bonding process and the SPR process were carried out respectively. **Table 2** lists the joint configurations for the interrupted tests. The specimen dimensions are presented in **Fig. 2**. The thicknesses of the top and bottom sheets are 1.2mm and 2.0mm respectively. The rivet selected for this stack is 6.0mm long with a shank diameter of Ø5.3mm. Each process was stopped at five positions by controlling the rivet head height (H_1). To verify the prediction accuracy of the simulation model, as shown in **Table 3**, another four types of SPR

joints and four types of Riv-Bonded joints with varying top sheet thicknesses and dies were also made experimentally. As for any mechanical fastening process, the intrinsic variability of the SPR and the Riv-Bonding processes inevitably bring many variations into the process and affect the final laboratory test results. To minimise such effects, the same equipment and the same dies as well as the same batch of materials were used throughout the experiment. In addition, at least two repeats for each position were made in the interrupted laboratory tests and three repeats for each joint in **Table 3** were performed when evaluating the performance of the simulation model. The nominal dimensions of the semi-tubular rivet and the die used in the laboratory tests are illustrated **Fig. 3**.

All the joints were made using a servo SPR system provided by Tucker GmbH, as shown in **Fig. 4**. The riveting speed is set to 300mm/s, and the clamping force is approx. 6.0kN controlled by a compressed spring. Due to the high viscosity (approx. 3000Pa • s) of the adhesive SikaPower 498 at the ambient temperature (shown in **Fig. 5**), the adhesive was preheated to about 55℃ to reduce its viscosity before manually applied on the bottom sheet. To keep consistent with the real application in the automotive industry, as shown in **Fig. 6**, the adhesive was applied along the centre line of the bottom sheet with a cartridge gun. The amount of the adhesive was controlled by the diameter of the gun nozzle (3.0mm). After the adhesive was applied on the bottom sheet, the top sheet was rapidly placed on the top of the adhesive followed by the riveting process as shown in **Fig. 1**(c). All the Riv-Bonded joints were placed in a preheated oven at 175℃ for 20 minutes to cure the adhesive layer.

Table 1 Properties of the adhesive SikaPower 498 (*SikaPower®*-498, 2016)

Name	Dynamic viscosity (Pa·s)		Application temperature (℃)	Curing time (min)	Elongation (After curing)
	20℃	55℃			
SikaPower 498	Approx. 3000	Approx. 1300	50~60	20 (175℃)	5.0%

Table 2 Configurations of the interrupted laboratory tests for the SPR and the Riv-Bonding processes

Test no.	Thickness (mm)		Adhesive SikaPower 498	Rivet head height/H_1 (mm)	Rivet (Boron steel)	Die
	Top sheet/T_t (AA5754)	Bottom sheet/T_b (AA5754)				
1-1	1.2	2.0	--	4.0	C5.3*6.0 (280±30HV10)	Pip die
1-2				3.0		
1-3				2.0		
1-4				1.0		
1-5				0.0		
2-1	1.2	2.0	Yes (Ø3.0mm nozzle)	4.0		
2-2				3.0		
2-3				2.0		
2-4				1.0		
2-5				0.0		

Table 3 Joint configurations for the simulation model verification

Test no.	Thickness (mm)		Adhesive SikaPower 498	Rivet (Boron steel)	Die
	Top sheet/T_t (AA5754)	Bottom sheet/T_b (AA5754)			
3-1	1.8	2.0	--	C5.3*6.0 (280±30HV10)	Pip die
3-2	2.5				
3-3	1.8				Flat die
3-4	2.5				
3-5	1.8	2.0	Yes (Ø3.0mm nozzle)	C5.3*6.0 (280±30HV10)	Pip die
3-6	2.5				
3-7	1.8				Flat die
3-8	2.5				

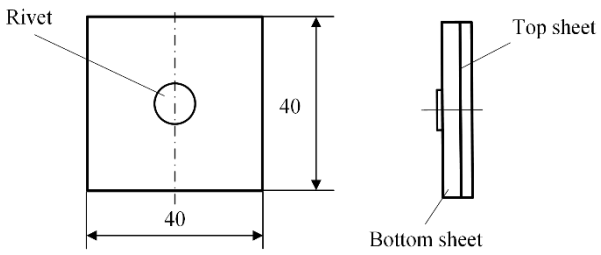

Fig. 2 Specimen dimensions of the SPR joint and the Riv-Bonded joint (in mm)

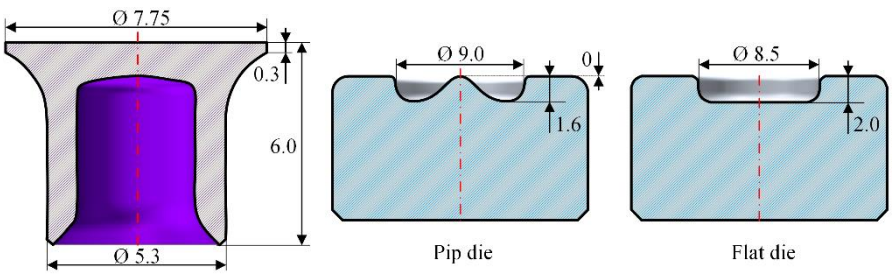

Fig. 3 Schematic of the semi-tubular rivet and dies (Dimensions in mm)

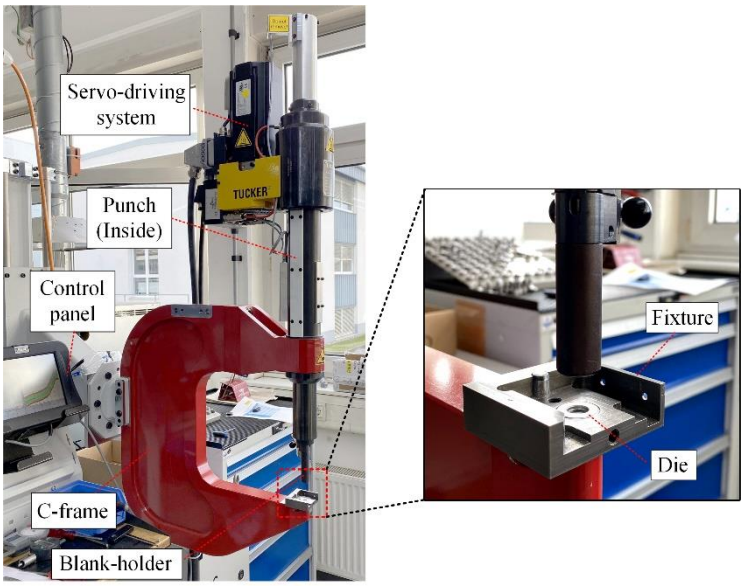

Fig. 4 Tucker SPR system

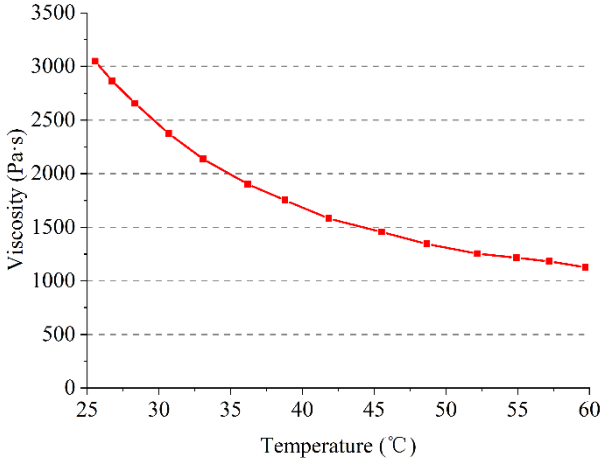

Fig. 5 Dynamic viscosity-temperature curve of the adhesive SikaPower 498 (*SikaPower*®-498, 2016)

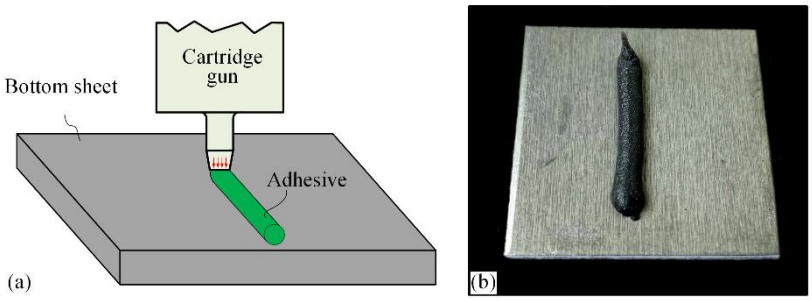

Fig. 6 Schematic of applying the uncured adhesive on the bottom sheet

2.2 Geometrical characterization of the SPR and the Riv-Bonded joints

To observe the adhesive distribution within the Riv-Bonded joints and to evaluate the joint quality, all the joints were sectioned using an abrasive-wheel cutting machine. To ensure the cross-sectional profile on the joint centre plane was captured, as shown in **Fig. 7**, the joints were sectioned at a position slight offset the joint centre line to reserve enough distance for the subsequent surface polishing. Then, the cross-sectional profile for each joint, as shown in **Fig. 8**, was inspected and recorded using an optical microscope. To evaluate the performance of the simulation model on the joint quality prediction, six dimensions as shown in **Fig. 9** were measured on the cross-sectional profiles of the SPR joint 1-5 and the Riv-bonded joint 2-5. The interlock (I_1), the rivet head height (H_1), the remaining bottom sheet thickness at the joint centre (t_1) and under the rivet tip (t_2) are the key joint quality indicators. The diameter of inner interlock boundary (D_1) and diameter of outer interlock boundary (D_2) are used to monitor the interlock formation and to evaluate the rivet shank deformation. **Table 4** lists the mean values of the six dimensions in the joints 1-5 and 2-5. The influences of the adhesive layer on the joining process and the joint quality were discussed in the following sections.

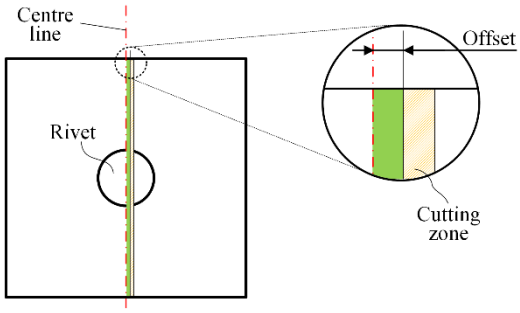

Fig. 7 Schematic of the cutting position on the specimen

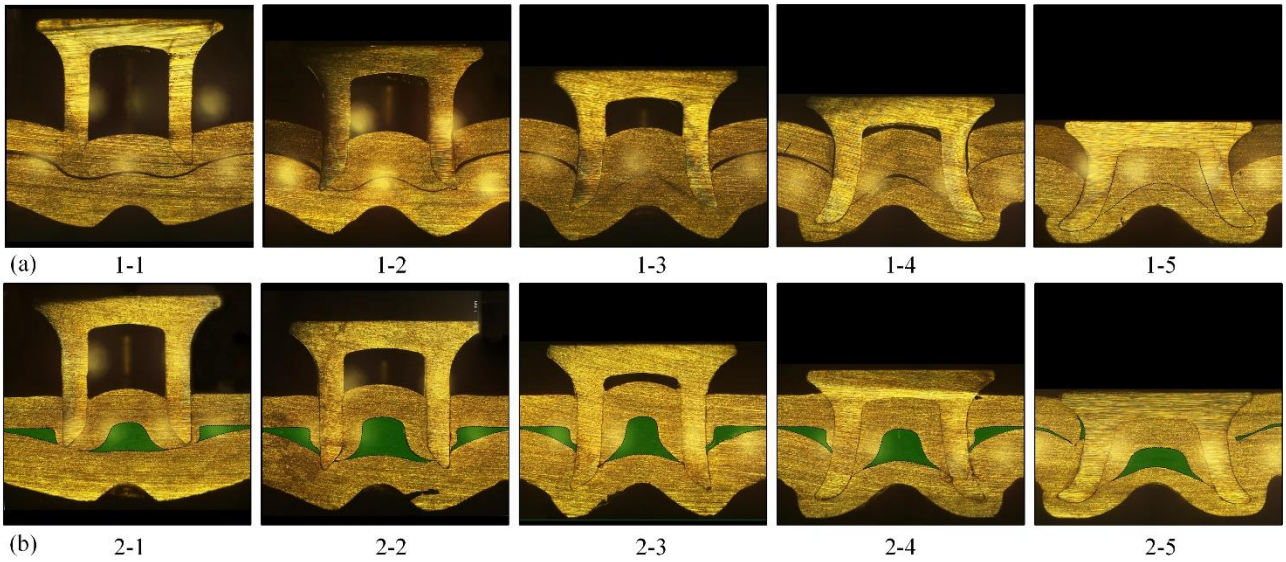

Fig. 8 Joint cross-sectional profiles during the (a) SPR process and (b) Riv-Bonding process

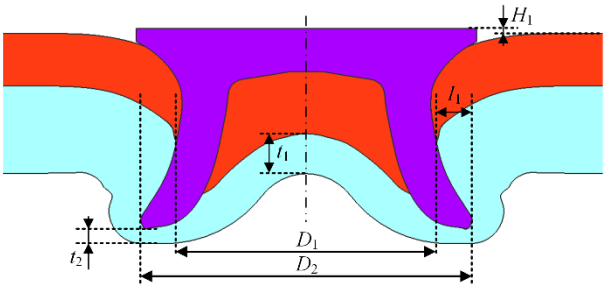

Fig. 9 Geometrical dimensions on the cross-sectional profile of the SPR or the Riv-Bonded joints

Table 4 Measured dimensions of the SPR joint 1-5 and the Riv-Bonded joint 2-5

Parameters	1-5		2-5	
	Mean	Standard deviation	Mean	Standard deviation
Rivet head height/H_1 (mm)	0.07	0.010	0.07	0.030
Interlock/I_1 (mm)	0.98	0.058	0.94	0.063
Bottom sheet thickness at the joint centre/t_1 (mm)	0.88	0.047	0.59	0.047
Bottom sheet thickness under the rivet tip/t_2 (mm)	0.56	0.150	0.53	0.040
Diameter of inner interlock boundary /D_1 (mm)	6.04	0.288	6.08	0.336
Diameter of outer interlock boundary/D_2 (mm)	8.00	0.260	7.95	0.324

3 Simulation model of the Riv-Bonding process

3.1 Model description

Due to the axisymmetric property of the Riv-Bonded joint, a 2D axisymmetric model was developed to meet the fast response requirement. Commercial software Simufact.Forming, developed by MSC Software Corporation, has a very strong re-meshing capability to handle large element distortions and was chosen in this study.

Fig. 10 shows the seven components involved in the simulation model: (1) punch; (2) blank-holder; (3) rivet; (4) top sheet; (5) adhesive layer, (6) bottom sheet and (7) die. To improve the model efficiency, the punch, blank-holder and die were modelled as rigid bodies. The rivet and the two sheets were modelled as elastic-plastic bodies. The adhesive layer was modelled as a superplastic body. Same quadrangle element with four gauss points (type 10) was chosen for these deformable components. The quadtree mesher, which could allocate more elements around the geometric boundaries, was selected to mesh the rivet. In contrast, the advancing front quad mesher, which could allocate regular elements on the whole part, was used to mesh the two sheets and the adhesive layer.

Usually, a fine mesh size can effectively reduce the mesh size influence and give a reliable simulation result. But the simulation time would increase rapidly with the decrease of the mesh size. To balance the simulation accuracy and the simulation time, in this study, a mesh size sensitivity study was performed (SPR joint: 1.5mm+1.5mm+ C5.3*5.0) to determine the suitable mesh sizes for the solid parts. **Fig. 11** shows the effects of different mesh sizes on the variations of the simulated joint quality indicators (i.e. the interlock I_1, the remaining bottom sheet thickness at the joint centre t_1 and under the rivet tip t_2) and the diameter of outer interlock boundary D_2. It can be seen that to achieve stable values of the quality indicators, the suitable global mesh sizes for the rivet, the top sheet and the bottom sheet were 0.10mm, 0.10mm and 0.12mm respectively. To further improve the model accuracy, the elements on the rivet shank and at the sheet central areas were locally refined to improve the model accuracy. The mesh size of the adhesive layer was set to 0.05mm to distribute enough elements along the thickness direction. During the riveting process, the two sheets undergo severe plastic deformations and the adhesive flows rapidly between the two sheets. This would lead to severe element distortion and convergence difficulty during the simulation. To resolve these issues, the automatic element re-meshing was implemented for the two sheets and the adhesive layer. No element re-meshing was applied on the rivet because it underwent limited deformation.

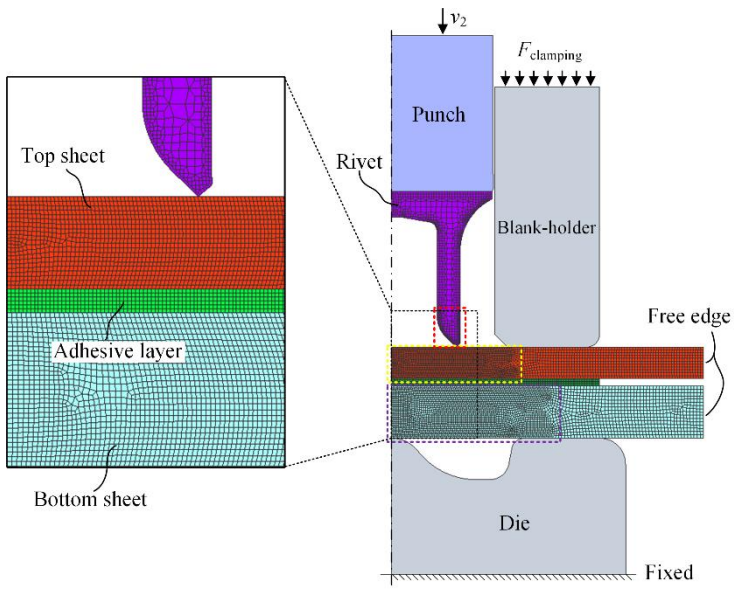

Fig. 10 2D axisymmetric simulation model of the Riv-Bonding process

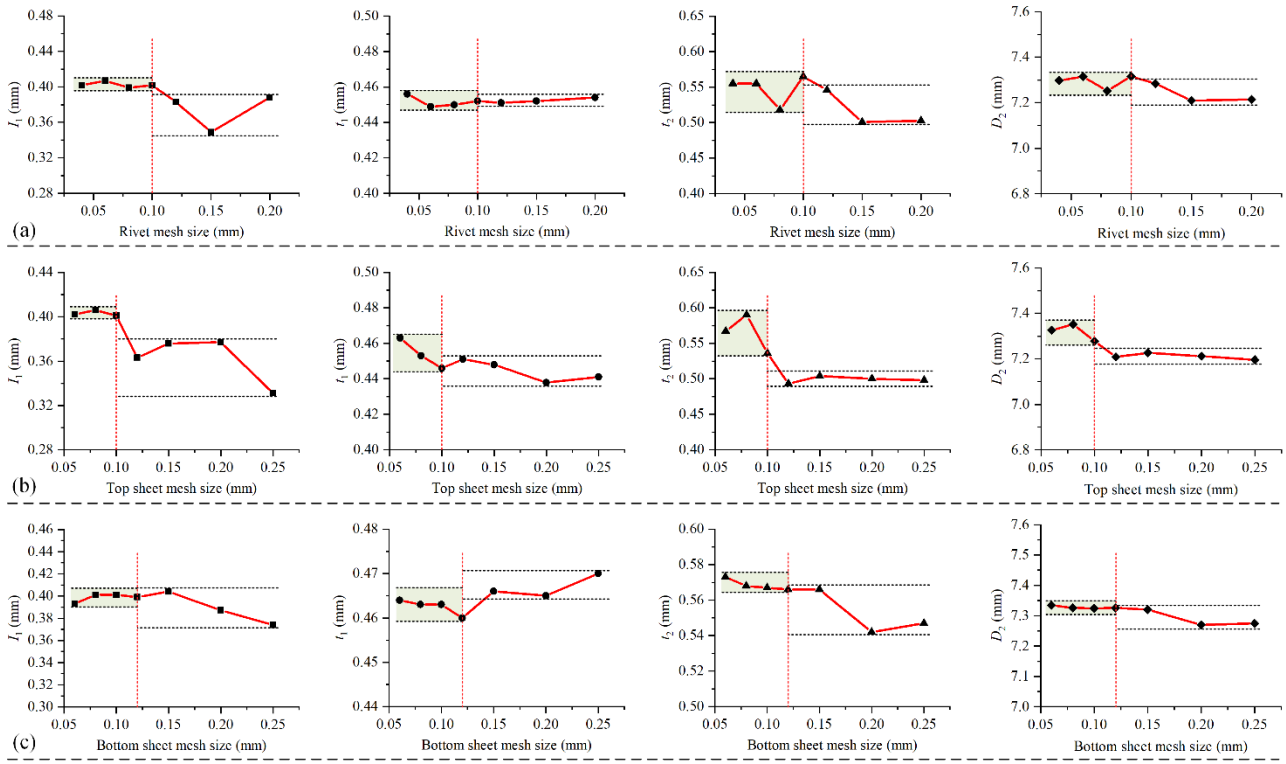

Fig. 11 Mesh size sensitivity results for (a) the rivet, (b) the top sheet and (c) the bottom sheet

The joining force F during the Riv-Bonding process (i.e. Riveting force F_r + Clamping force $F_{clamping}$) can reach to a very high value (approx. 60kN~80 kN). This would lead to C-frame deflection and result in a downward movement of the die, as shown in **Fig. 12**. The deflection angle of the C-frame α_1 could be roughly calculated using the die displacement along the vertical direction L_1 and the length of the cantilever L_2 in Eq.(1). According to the experimentally recorded load-displacement curve, the L_1 is only several millimetres. It is much smaller than the L_2 (approx. 250mm). As a result, the deflection angle will be a very small value. For instance, given that the L_1 and L_2 are 3.0mm and 250mm respectively, the

calculated α_1 would be just 0.69°. Hence, the die movement could be simplified to a pure vertical movement and modelled easily by applying a high stiffness spring underneath the die in Simufact.Forming. However, by comparing the simulation results with or without considering the die movement, it was found that there is no obvious difference. Instead, a longer simulation time was needed when considering the die movement because of the larger rivet displacement. Therefore, the die movement induced by the C-frame deflection was not considered in the current model.

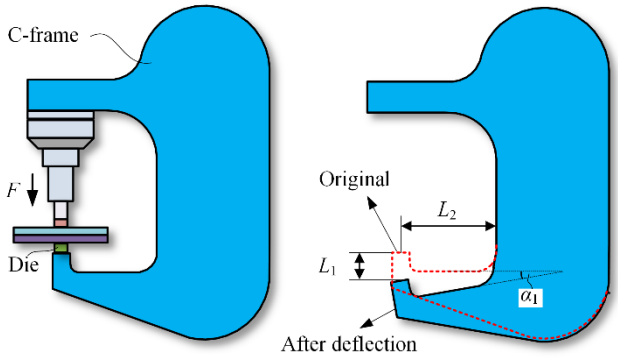

Fig. 12 Schematic of the C-frame deflection under a high joining force

$$\alpha_1 = \arctan \frac{L_1}{L_2} \cdot \frac{180°}{\pi} \tag{1}$$

During the Riv-Bonding process, the top sheet and the adhesive layer would be penetrated by the rivet. To model this phenomenon, a geometrical criterion was implemented. Once the thickness of the top sheet or the adhesive layer reduces to the predefined critical minimum values, material separation would be implemented with the assistance of the advancing front quad mesher. This critical thickness value has significant impacts on the simulation result. For the top sheet, it would fracture very early with a large critical value but undergo an unrealistic deformation with a very small critical value. Both cases would affect the interlock value by altering the contact point between the rivet shank and the bottom sheet. For the adhesive layer, too large critical value would cause unrealistic adhesive separation and very large adhesive volume loss caused by the element deletion. In this model, these critical values were determined using the inverse method (i.e. by comparing the simulated and laboratory tested joint cross-sectional profiles). The critical thicknesses for the top sheet and the adhesive layer were set to 0.04mm and 0.03mm respectively.

Different contact models were implemented in this model. For the contact between solid parts, the Coulomb friction model was selected to calculate the friction at the contact interfaces. Due to the difficulties to experimentally measure the friction coefficient, the inverse method was adopted. The friction coefficient between the die and the bottom sheet was set to 0.22, while between other solid parts was set to 0.10. For the interaction between the adhesive and other solid parts, the two sheets and the adhesive layer were glued together using the contact type ‘Glued’. The contact interface between the adhesive and the rivet was modelled as a friction free condition by setting the friction coefficient to zero. To keep

consistent with the experimental conditions, the punch velocity (v_2) and the clamping force ($F_{clamping}$) on the blank-holder were set to 300mm/s and 6.0kN respectively.

During the Riv-Bonding process, the blank-holder moved downward with an initial speed, and struck on the top sheet. Then, a clamping force was applied on the blank-holder by a compressed spring. This clamping procedure had significant effects not only on the adhesive distribution, but also on the deformation of the top sheet. **Fig. 13** shows the cross-sectional profiles of the SPR joint 1-1 and the Riv-bonded joint 2-1 (the rivet head height H_1= 4.0mm). It can be found that the top sheet outside the rivet bent downward during the SPR process (zone 1), but kept almost flat during the Riv-Bonding process (zone 2). This difference indicated that the top sheet in the Riv-Bonding process first bent upward due to the hydraulic force introduced by the accumulated adhesive beneath its central area, but then became almost flat as the riveting process proceeded as shown in **Fig. 13**(b). Therefore, according to the adhesive distribution, the clamping process during the Riv-Bonding process could be divided into two stages as presented in **Fig. 14**. At stage 1, the gap between the two sheets is quite large and the adhesive could easily flow towards the outside of the interface. The sheets undergo very limited elastic deformation due to the low-level pressure from the adhesive layer. Almost uniform adhesive distribution can be observed during this stage. However, with further downward movement of the blank-holder, the gap between the two sheets becomes narrower and the outward flow of the adhesive becomes more and more restricted. At stage 2, the adhesive starts being trapped around the joint centre and less adhesive remains under the circular edge of the blank-holder. Plastic deformations occur on the two sheets due to the hydraulic pressure from the trapped adhesive. During this stage, the adhesive unevenly distributes between the two sheets.

To properly simulate the blank-holder strike and to simplify the simulation model, in this study, the clamping process was simulated from the beginning of the stage 2. The initial adhesive layer thickness was determined using the inverse method and set to 0.3mm. The simulation procedures of the Riv-Bonding process are shown in **Fig. 15**. When simulating the clamping process, the blank-holder first moves 0.3mm at a velocity 100mm/s to model the blank-holder strike on the stack. Then, the blank-holder velocity is set to zero and a 6.0kN clamping force ($F_{clamping}$) is applied to model the blank-holder clamping effect. Subsequently, the riveting process is simulated.

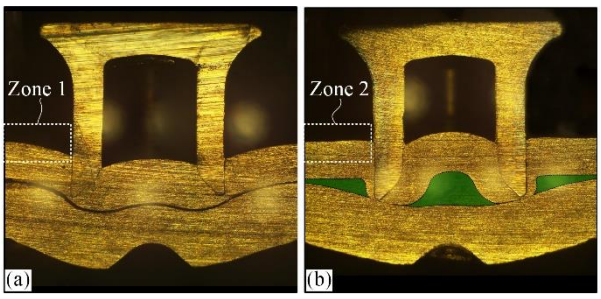

Fig. 13 Deformed top sheets at the rivet head height H_1=4.0mm: (a) the SPR joint 1-1 and (b) the Riv-Bonded joint 2-1

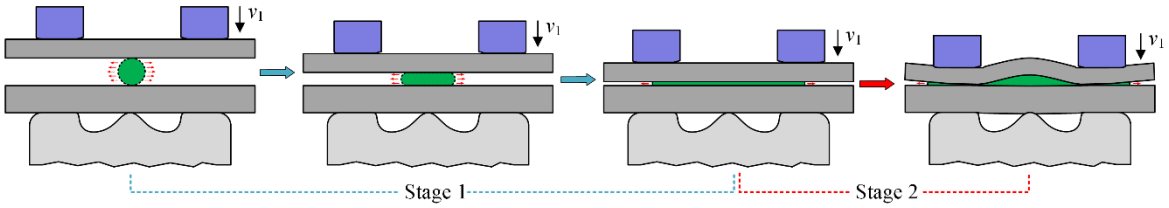

Fig. 14 Two stages of the adhesive flow during the clamping process

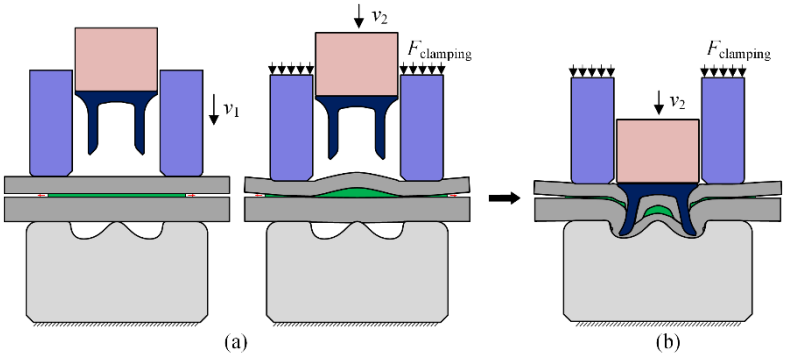

Fig. 15 Simulation procedures of the Riv-Bonding process: (a) Clamping process and (b) Riveting process

3.2 Material attributes

The material constitutive models are very important for the simulation model development. In this study, all the rivet and sheets are characterized using plastic stress-strain curves. The plastic stress-strain curves of the aluminium alloy AA5754 (Strain rate=1s^{-1}) extracted from (Carandente et al., 2016) were employed, and the temperature effect on the sheet strength was considered as shown in **Fig. 16**. Due to the relatively low strain rate that a standard tensile test can reach, the strain rate effect on the material strength was not considered. Carandente et al. (2016) measured the temperature inside the joining zone and found that the maximum temperature was always lower than 250°C throughout the riveting process. This temperature variation has very little impact on the mechanical strength of the boron steel. Therefore, only the plastic stress-strain curve under strain rate 0.01s^{-1} at 20°C was implemented for the rivet as shown in **Fig. 17**.

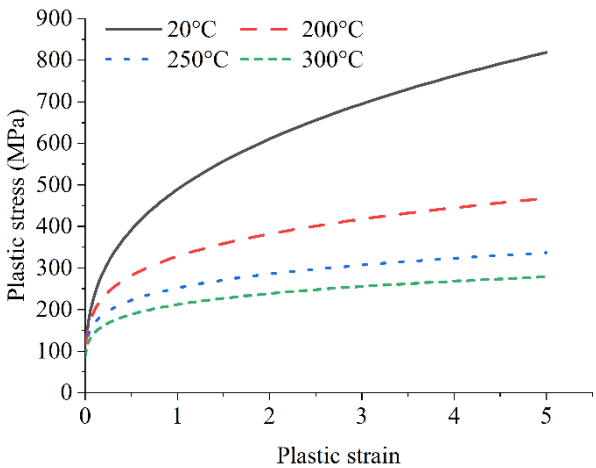

Fig. 16 Plastic stress-strain curves of the aluminium alloy AA5754 at different temperatures (Strain rate=1s^{-1}) (Carandente et al., 2016)

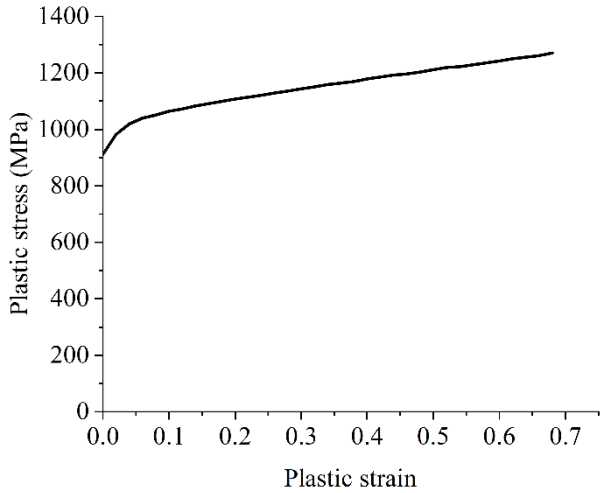

Fig. 17 Plastic stress-strain curve of the boron steel (Strain rate=0.01s^{-1}, 20°C)

The properties of the uncured adhesive (SikaPower 498) is quite different from that of the rivet and the sheets. It demonstrates a viscoelastic behaviour depending heavily on the dynamic viscosity. This adhesive is a non-Newtonian fluid and its viscosity shows a decreasing trend with the increment of the strain rate (i.e. pseudoplastic fluid). The adhesive flow between the two sheets is quite simple, and regarded as a laminar flow in this study. The Ostward and de Waele power law, which was proved capable for the modelling of power law fluids by Jabbari et al. (2013), was adopted to describe the relationships between the shear stress (τ) and the shear strain rate ($\dot{\gamma}$) of the adhesive layer, as shown in Eq.(2). The coefficients *k* and *n* could be easily identified using rheological experiments. The dynamic viscosity (η) of adhesive depends heavily on the shear strain rate, and can be expressed as a function of the shear stress (τ) and shear strain rate ($\dot{\gamma}$) in Eq.(3). Substituting Eq.(2) into Eq.(3) yields the dynamic viscosity (η) as a function of the shear strain rate ($\dot{\gamma}$) in Eq.(4).

$$\tau = k\dot{\gamma}^{n} \tag{2}$$

$$\eta = \frac{\tau}{\dot{\gamma}} \tag{3}$$

$$\eta = k\dot{\gamma}^{n-1} \tag{4}$$

In this study, the experimental viscosity data of the adhesive SikaPower 498 was extracted from the paper of Weber et al. (2011). **Fig. 18** shows the shear stress-viscosity curves at different temperatures. Using the Eq.(3), the adhesive viscosity under varying shear strain rate was derived and presented in **Fig. 19**. In this model, only the shear strain rate-viscosity curve at 50° C was implemented. By employing the least squares technique, the unknown coefficients in Eq.(4) were identified. Values of the *k* and *n* are 1582.04 and 0.23 respectively. However, this fitted shear rate-viscosity curve has very small viscosity values (Less than 2.0Pa • s) at very high strain rates (Greater than 5000 s^{-1}), which is not coincident

with the reality and also causes simulation stability problems in Simufact.Forming. So the index *n* was adjusted to a larger value 0.48 by using the inverse method. The viscosity of SikaPower 498 at 50° C under different shear strain rates was defined in Eq.(5).

$$\eta = 1582.04 \cdot \dot{\gamma}^{-0.52} \tag{5}$$

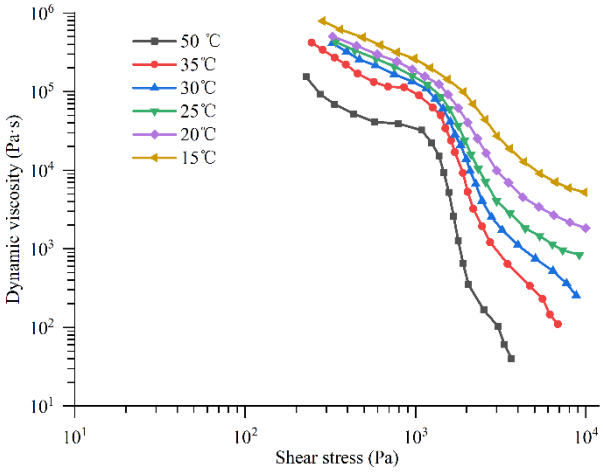

Fig. 18 Shear stress-viscosity curves of the adhesive SikaPower 498 at different temperatures (Weber et al., 2011)

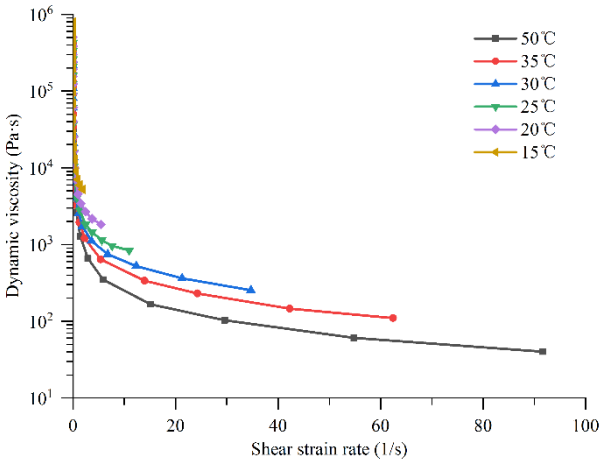

Fig. 19 Shear strain rate-viscosity curves of the adheisve SikaPower 498 at different temperatures

The adhesive was modelled as a superplastic material using the rate-power law constitutive model shown in Eq.(6) (Hot forging material form 1 in Simufact.Forming). By setting the coefficient *N* to zero, the effect of equivalent strain ($\bar{\varepsilon}$) on the equivalent stress (σ_f) was inactive and the Eq.(6) is simplified to Eq.(7). The shear stress (τ) and the shear strain rate ($\dot{\gamma}$) could be expressed as a function of equivalent stress (σ_f) and equivalent strain rate ($\dot{\bar{\varepsilon}}$) individually in Eq.(8) and Eq. (9) according to the study of Gerstmann and Awiszus (2020).

$$\sigma_f = C\dot{\bar{\varepsilon}}^M \bar{\varepsilon}^N \tag{6}$$

$$\sigma_f = C\dot{\bar{\varepsilon}}^M \tag{7}$$

$$\tau = \frac{\sigma_f}{\sqrt{3}} \tag{8}$$

$$\dot{\gamma} = \sqrt{3} \cdot \dot{\bar{\varepsilon}} \tag{9}$$

Substituting the Eq.(8) and Eq.(9) into Eq.(2) yields Eq.(10). Comparing the Eq.(7) and Eq.(10), the coefficients *C* and *M* could be expressed as a function of *k* and *n* shown in Eq.(11). Substituting the identified *k* and *n* into Eq.(11), the equivalent stress-strain rate curve of the adhesive SikaPower 498 could be deduced into Eq.(12) and illustrated in **Fig. 20**.

$$\sigma_f = \sqrt{3}^{n+1} \cdot k \cdot \dot{\bar{\varepsilon}}^n \tag{10}$$

$$\begin{cases} C = \sqrt{3}^{n+1} \cdot k \\ N = n \end{cases} \tag{11}$$

$$\sigma_f = 3143.53 \cdot \dot{\bar{\varepsilon}}^{0.48} \tag{12}$$

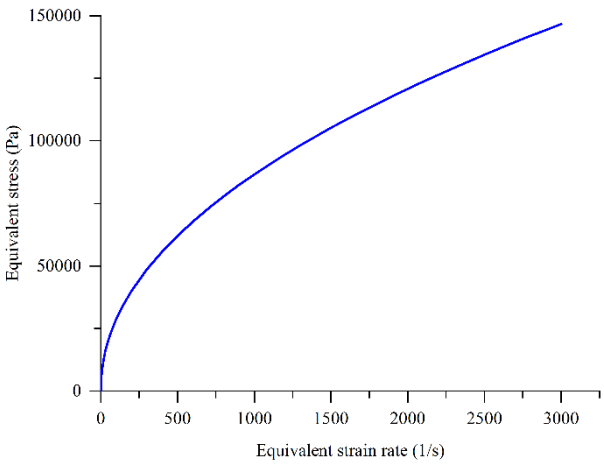

Fig. 20 Equivalent stress-strain rate curve of the adhesive SikaPower 498 (50° C)

3.3 Model verification

To evaluate the performance of the developed simulation model, the SPR/Riv-Bonded joints in **Table 2** and **Table 3** were numerically made and compared with the experimental test results, including the joint cross-sectional profiles at different joining stages, the values of joint quality indicators and the load-displacement curves. All the simulations were executed on a PC with a 4-core Intel Core i7 3.4GHz CPU and RAM 16.0G. Four cases were simulated at the same time, and could be finished within 50mins.

Fig. 21 compares the experimentally tested and digitally simulated joint cross-sectional profiles at five positions during the SPR process. It is apparent that the deformations of the sheets and the rivet at each position were accurately predicted. As shown in zone 1 and zone 2, the separation of top sheet was accurately simulated using the geometrical criterion

(critical value=0.04mm). The gap formed between the two sheets (zone 3 and zone 4) and even the material folds on the bottom sheet (zone 5 and zone 6) were also captured by the simulation model. The dimensions of the quality indictors measured on the tested and the simulated cross-sectional profiles of the SPR joint 1-5 are presented in **Fig. 22**. The predicted interlock (I_1) is approximately 82% of the average interlock value extracted from the laboratory tested samples. The diameters of the two interlock boundaries (D_1 and D_2) were accurately predicted with relative errors lower than 5% of the tested values. The predicted rivet head height is around 86% of the tested value. This 14% relative error is mainly caused by the small value of the tested rivet head height (H_1=0.07mm). The small absolute error (0.01mm) between the simulated (0.06mm) and tested (0.07mm) rivet head height led to this large relative error. For the bottom sheet, the remaining thickness around the joint centre (t_1) was accurately predicted and the relative error is smaller than 5% of the tested value. While the thickness under the rivet tip (t_2) was underestimated by the simulation model, and the predicted thickness is only 65% of the tested value. **Fig. 23** shows the final tested and simulated cross-sectional profiles of the SPR joint 1-5. Except for the underestimated remaining bottom sheet thickness under the rivet tip (t_2), the simulation result shows a good agreement with the laboratory test.

The load-displacement curves during the whole SPR processes were extracted from both of the laboratory tested and the simulated SPR joint 1-5, as shown in **Fig. 24**. The effect of C-frame deflection on the tested load-displacement curve was removed using Eq.(13). The s_t is the true rivet displacement relative to the die, and the s_a is the recorded rivet displacement during the joining process. The F_r is the riveting force during the SPR process. The calibrated C-frame stiffness K of the SPR system used in this study is approx. 21kN/mm. It can be seen that the simulated curve (black line) matches well with the tested true curve (red line). The tested curve started around 5.0kN rather than 0kN. This is because the SPR system detects the contact between the top sheet and the rivet once the measured force on the rivet reaches certain value (approx. 5.0kN in this case). So there is a displacement offset and a riveting force offset between the starting points of the tested and the simulated curves. The slightly decline in zone 2 and the sudden change of the growth rate of the riveting force in zone 3 were accurately predicted by the developed simulation model.

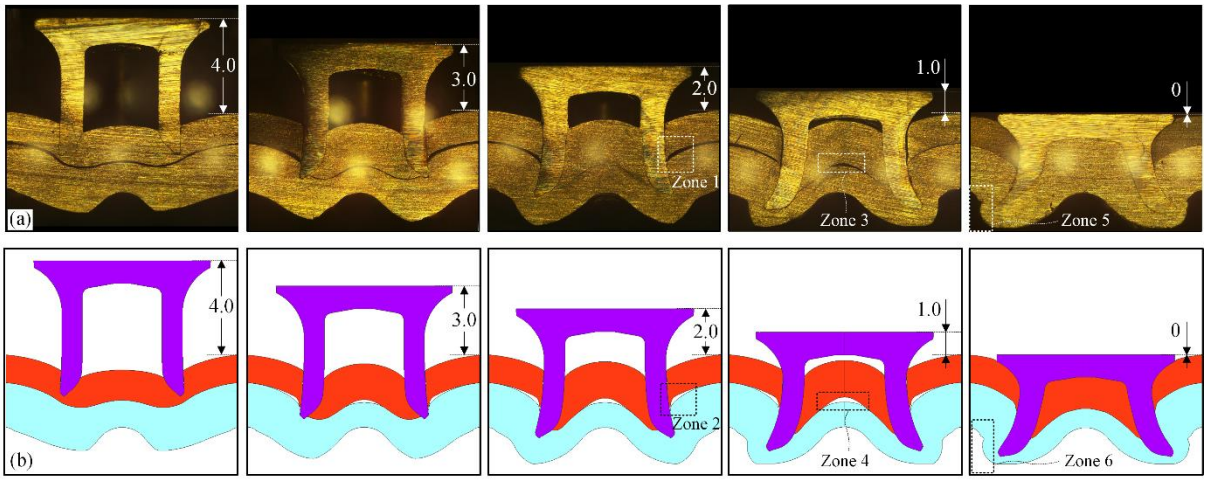

Fig. 21 Comparison of the joint cross-sectional profiles during the SPR process (a) Interrupted laboratory tests and (b) Simulations

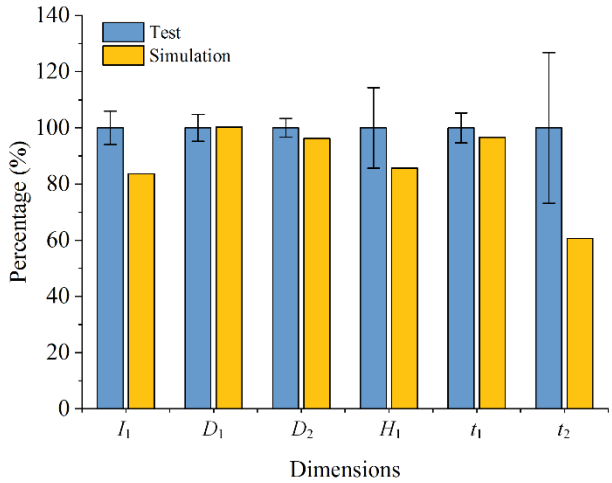

Fig. 22 Comparison of the SPR joint 1-5 quality indicators between the laboratory tests and the simulation

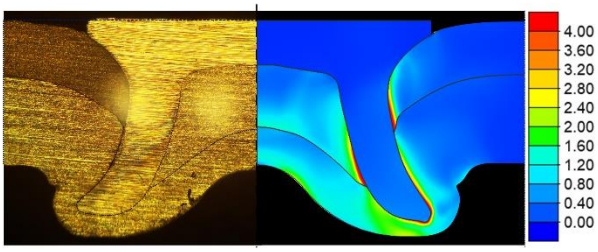

Fig. 23 Simulated and tested cross-sectional profiles of the SPR joint 1-5 (Effective plastic strain)

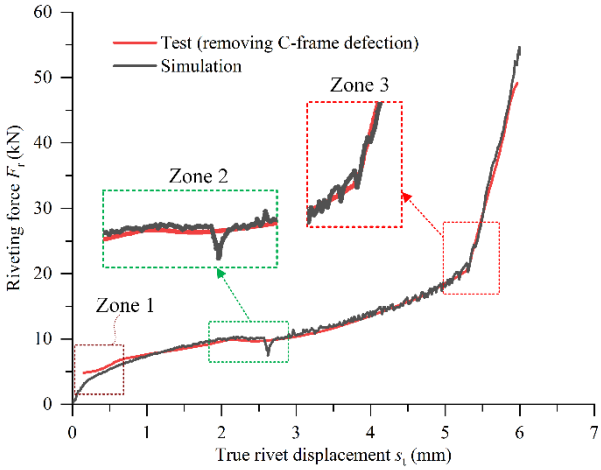

Fig. 24 Simulated and tested true load-displacement curves of the SPR joint 1-5

$$s_t = s_a - \frac{F_r}{K} \tag{13}$$

Fig. 25 presented the experimentally tested and digitally simulated joint cross-sectional profiles at five positions during the Riv-Bonding process. To highlight the effect of the blank-holder strike on the simulation result of the Riv-Bonding process, the simulated joint cross-sectional profiles considering (model 1) and without considering (model 2) the blank-holder strike are compared with that from the laboratory tests. It is obvious that the simulation result considering the blank-holder strike (**Fig. 25**(b)) had a much better agreement with the laboratory result (**Fig. 25**(a)) than that without considering the blank-holder strike (**Fig. 25**(c)). When the rivet penetrated the top sheet, the deformation of the top sheet material around the rivet tip (zone 1) and the adhesive distribution under the top sheet (zone 4) were accurately predicted by the simulation model 1 (zone 2 and 5). The flat top sheet (zone 7) and the final adhesive distribution (zone 10) were also captured by the simulation model 1 (zone 8 and 11). In contrast, although the model 2 captured the adhesive distribution around the joint centre, the deformation of the top sheet and the adhesive distribution outside the joining region were not properly simulated. As shown in **Fig. 26**, the top sheet deflection caused by the adhesive layer was also accurately captured when considering the blank-holder strike in the simulation model (model 1). Therefore, in this study, the blank-holder strike was considered when developing the simulation model of the Riv-Bonding process.

To assess the accuracy of quality prediction of the developed model for the Riv-bonded joint, the dimensions of the quality indicators measured from the laboratory tested and the simulated cross sectional profiles of the Riv-bonded joint 2-5 are compared as shown in **Fig. 27**. It can be seen that there is a reasonable agreement between the simulated and the tested values. The simulated interlock is 80% of the tested value, and the simulated diameters of the two interlock boundaries (D_1 and D_2) are approximately 98% and 95% of the tested values. The simulated rivet head height is about 94% of the tested value. The bottom sheet thickness around the joint centre (t_1) was around 15% overestimated, and the remaining bottom sheet thickness under the rivet tip (t_2) was around 30% underestimated by the developed simulation model. The

tested and simulated cross-sectional profiles of the Riv-Bonded joint 2-5 are shown in **Fig. 28**. Apart from the bottom sheet thickness under the rivet tip, the simulated adhesive distribution and the sheet deformation agreed well with the laboratory tested results. **Fig. 29** compares the true load-displacement curves extracted from the simulated and tested Riv-bonded joint 2-5. The C-frame deflection effect on the tested curve was removed. It can be found that, except for the slight difference in zone 3, the predicted load-displacement curve (black line) matches well with the tested curve (red line). The slight decline (zone 1) and the rapid increase (zone 2) of the riveting force were accurately captured by the simulation model.

The above results and analysis have indicated that the developed simulation model with considering the blank-holder strike is capable of not only predicting the Riv-Bonding process but also the SPR process.

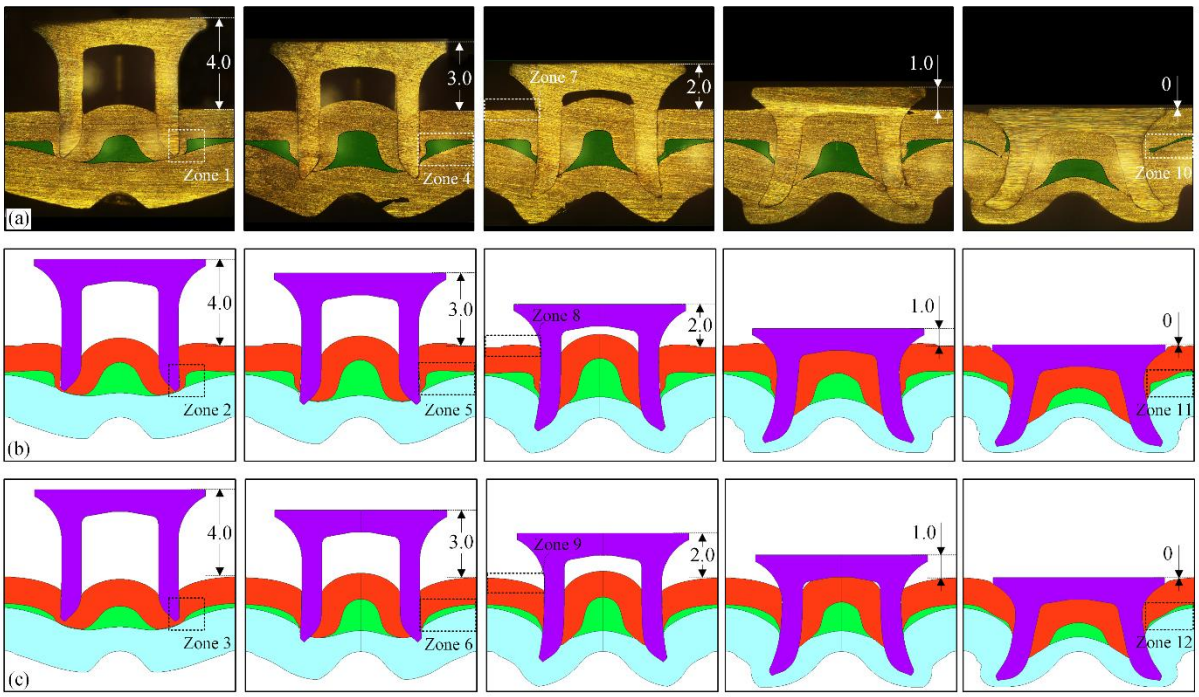

Fig. 25 Comparison of the joint cross-sectional profiles during the Riv-Bonding process (a) the interrupted laboratory tests (b) simulaiton with considering the blank-holder strike (c) simulation without considering the blank-holder strike

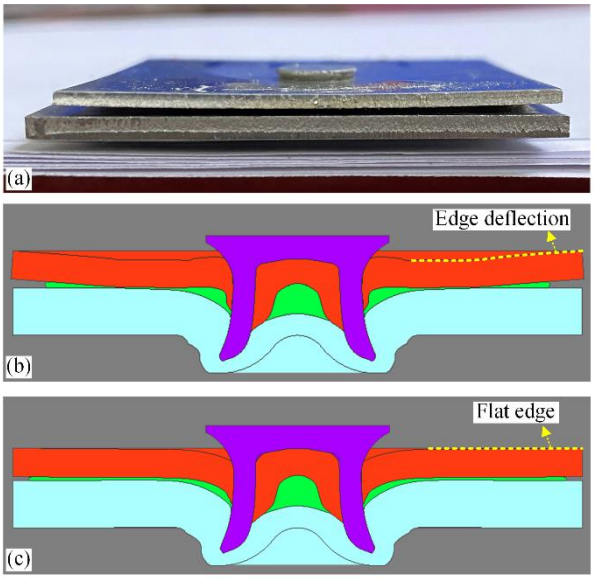

Fig. 26 Shapes of the Riv-Bonded joint 2-4: (a) Tested; (b) Simulated with or (c) without considering the blank-holder strike (H_1=1.0mm)

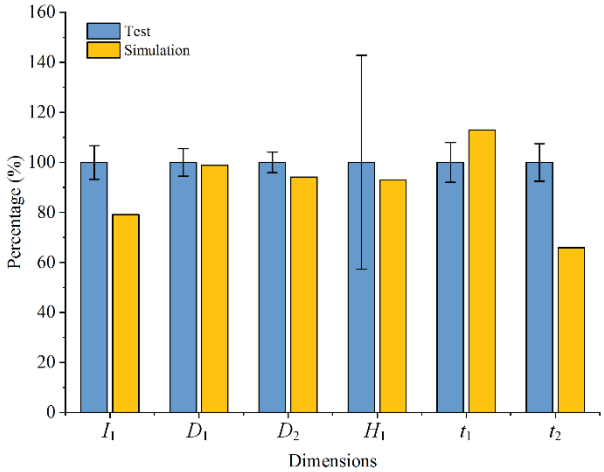

Fig. 27 Comparison of the Riv-Bonded joint 2-5 quality indicators between the laboratory tests and the simulation

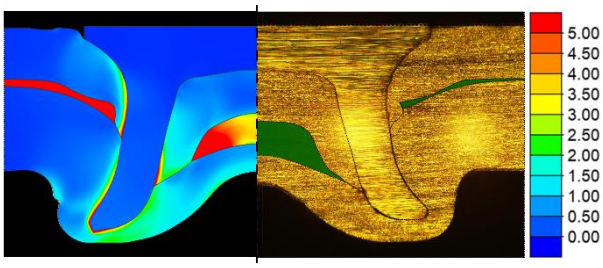

Fig. 28 Simulated and tested cross-sectional profiles of the Riv-Bonded joint 2-5 (Effective plastic strain)

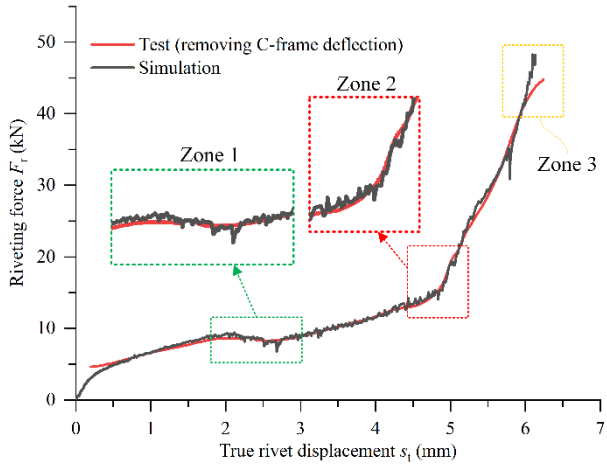

Fig. 29 Simulated and tested true load-displacement curves of the Riv-Bonded joint 2-5

To further verify the performances of the developed simulation model for different joint configurations, the simulated and experimentally tested cross-sectional profiles of the eight types of joints in **Table 3** were compared in **Fig. 30**. It can be seen that the simulated rivet and sheets deformations matched well with that from the experimental tests. Meanwhile, the predicted adhesive distributions in the Riv-Bonded joints also showed reasonable agreements with that in the tested Riv-Bonded joints. **Fig. 31** compared the simulated and tested joint quality indicators, including the interlock, the remaining bottom sheet thickness at the joint centre (t_1) and under the rivet tip (t_2), the diameter of outer interlock boundary (D_2). With varying top sheet thicknesses and die types, the changing trends of these indicators were accurately predicted by the simulation model. The predicted magnitudes of these indicators also showed reasonable agreements with that from the experimental tests. **Fig. 32** shows the simulated and tested true load-displacement curves. It can be noticed that, no matter with or without the adhesive layer, the changing trend and the magnitude of the riveting force were accurately predicted by the developed simulation model. Therefore, the developed simulation model is also capable of predicting the quality of SPR joints and Riv-Bonded joints with varying joint configurations.

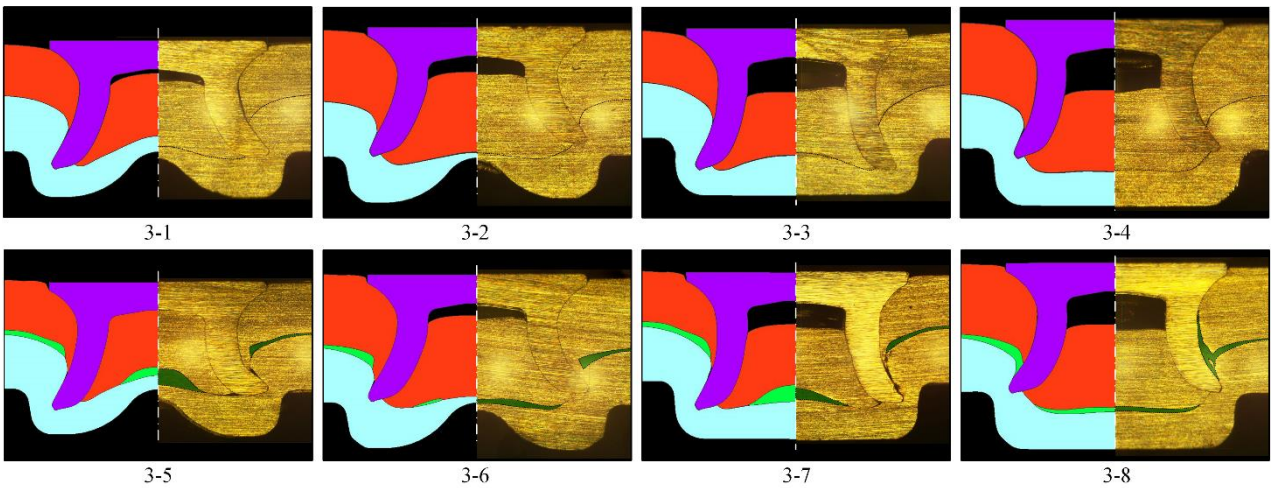

Fig. 30 Simulated and tested joint cross-sectional profiles for model validation

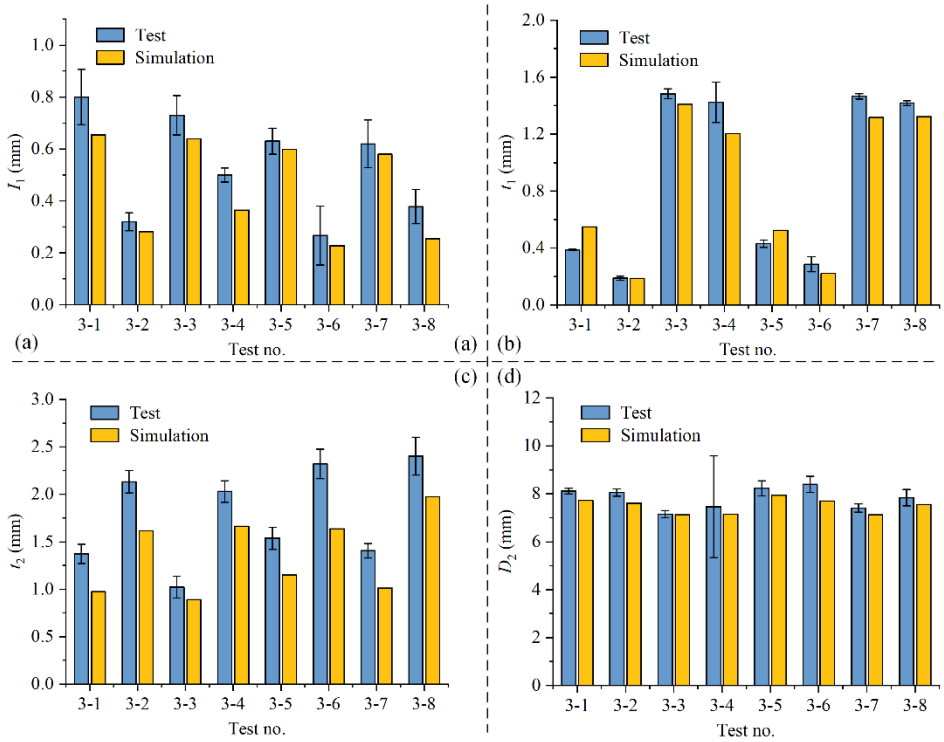

Fig. 31 Comparison of critical quality indicators between the experimentally tested and simulated joints

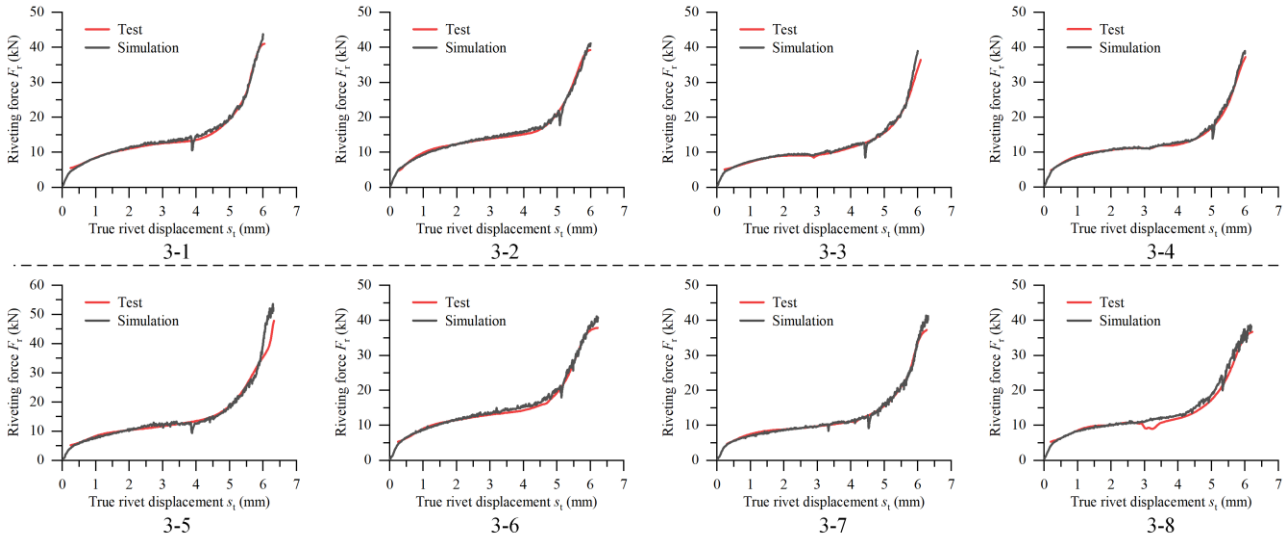

Fig. 32 Simulated and tested true load-displacement curves for model validation

4 Experimental investigation on the influences of the adhesive layer

As for any simulation, certain pre-defined conditions are required for model development, but not necessary 100% match the situation in real life. For example, the adhesive temperature would be affected by the thermal conductivity of the aluminium sheets, the ambient temperature and the time spent during the riveting process. Due to such limitations, this section uses experimental data to analyse in detail the adhesive effects on the riveting process, the load-displacement

curves and the joint quality. Certain features observed from the experimental data, like, trapped adhesive, deformation of the sheets, the rivet, even the nose on the top sheet, are matched well with the simulated profiles, but not mentioned in the following discussion in order to maintain the focus of this discussion.

4.1 Influences on the riveting process

The cross-sectional profiles of the laboratory tested joints during the SPR and the Riv-Bonding processes are compared in **Fig. 33**. It can be seen that the deformation behaviour of the rivet and the two sheets in the Riv-Bonding process was obviously different from that in the SPR process, especially the top sheet. This is undoubtedly attributed to the trapped adhesive between the two sheets, which introduced a hydraulic force leading to a different riveting process. The riveting force, which is closely associated with the deformation of the rivet and the sheets, also differed. **Fig. 34** shows the comparison between the true load-displacement curves extracted from the SPR process of the joint 1-5 (black line) and from the Riv-Bonding process of the joint 2-5 (red line).

As mentioned above, during the clamping stage of the Riv-Bonding process, the trapped adhesive around the joint centre introduced a noticeable hydraulic pressure on the central area of the top sheet leading to a locally upward movement of the top sheet. As a result, when the top sheet was almost penetrated as shown in **Fig. 33**(a-1), the top sheet became almost flat (red dash line). In contrast, during the SPR process, the clamping stage had less influence on the top sheet and it therefore bent downward (blue dash line) under the pressure from the rivet as shown in **Fig. 33**(b-1). During this period, a slightly smaller riveting force was observed in the Riv-Bonding process as shown in **Fig. 34**. This is attributed to the longer piercing time of the top sheet due to the higher initial top sheet position in the Riv-Bonding process. At the same rivet displacements, the rivet penetrated less into the top sheet and hence encountered less resistance than in the SPR process. The slowly outward adhesive flow also a possible reason for this smaller riveting force. Moreover, as shown in **Fig. 33**(a-2), the top sheet around the rivet shank was stretched for a longer distance and a nose was formed for the Riv-Bonding process, whilst less deformation of the top sheet at the same position for the SPR process, as shown in **Fig. 33**(b-2). By comparing the **Fig. 33**(a-3) and (b-3), a much larger deformation of the top sheet inside the rivet cavity was observed during the Riv-Bonding process. This is mainly caused by the fluidity of the uncured adhesive and the hydraulic pressure introduced by the trapped adhesive. The existence of the adhesive led to an earlier filling up of the rivet cavity in the Riv-Bonding process as shown in **Fig. 33**(a-4), compared to the SPR process as shown in **Fig. 33**(b-4). The fully filled material inside the rivet cavity imposed a much larger resistance on the downward movement of the rivet, which led to a rapid increase of the riveting force. As a result, the riveting force increased rapidly at an earlier time in the Riv-Bonding process (point *A*) compared to the SPR process (point *B*) as shown in **Fig. 34**.

At the end of the Riv-Bonding process, a very thin adhesive layer was left between the two sheets outside the rivet as presented in **Fig. 33**(a-5). This is because under the high riveting force, part of the adhesive outside the rivet was squeezed outwards once the rivet head started contacting the top sheet. Meanwhile, the nose formed on the top sheet was partially pressed into the bottom sheet and increased the diameter of the inner interlock boundary (D_1). This phenomenon has a negative effect on the interlock formation. As shown in **Fig. 33**(a-4), the n-shape top sheet and the uncured adhesive trapped in the rivet cavity were easier to be deformed and pressed downward than the sheet materials filled in the rivet cavity shown in **Fig. 33**(b-4). The liquid adhesive also demonstrated a lubricant effect to reduce frictions at the contact interfaces. So the growth speed during the rapid increasing phase in the Riv-Bonding process was smaller than that in the SPR process. As a result, the maximum riveting force during the Riv-Bonding process is about 5.0kN smaller than that during the SPR process as presented in **Fig. 34**.

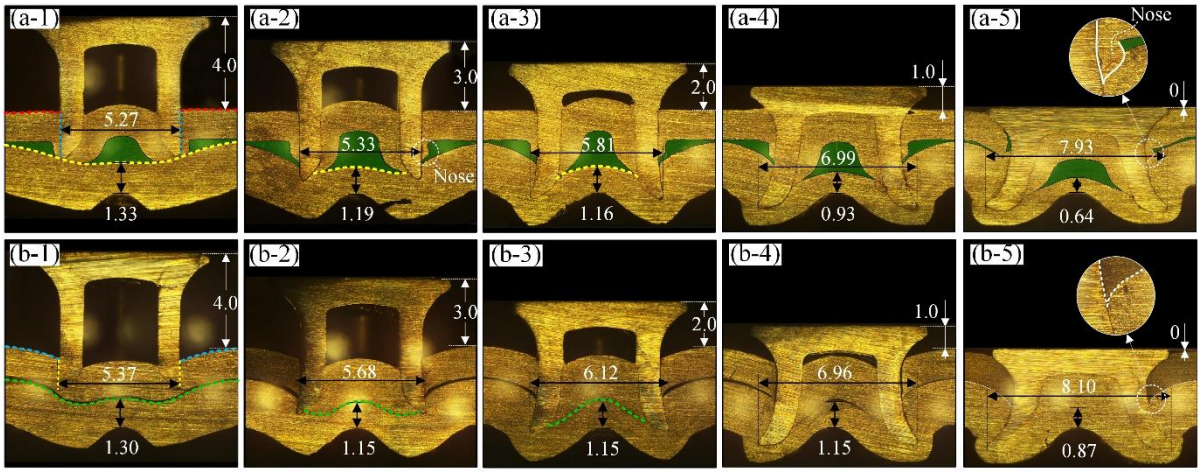

Fig. 33 Comparison between the joint cross-sectional profiles during the (a) Riv-Bonding process and (b) SPR process

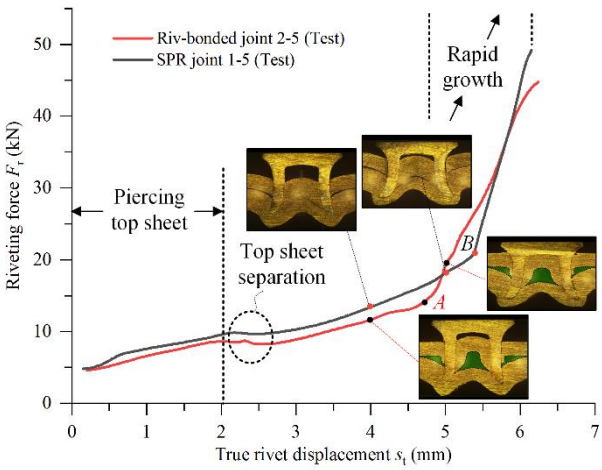

Fig. 34 Tested true load-displacement curves of the SPR joint 1-5 and Riv-Bonded joint 2-5

Although the deformation of the bottom sheet is mainly governed by the die profile, the existence of the adhesive layer also demonstrated apparent influences. As discussed previously, during the Riv-Bonding process, the top sheet inside the

rivet cavity underwent a larger deformation and moved upward as shown in **Fig. 33**(a-1)(a-2)(a-3). This resulted in a smaller top surface curvature of the bottom sheet (Yellow lines) compared with that in the SPR process (Green lines) as shown in **Fig. 33**(b-1)(b-2)(b-3). The changing curves of the bottom sheet thickness at the joint centre (t_1) during the two processes are shown in **Fig. 35**(a). Similar decreasing patterns were observed on the two curves. It first decreased rapidly at the early stage, and then kept almost constant for a period before the second rapid decline occurred. The values of the t_1 were almost coincident between the two processes during the first rapid decline and the unchanged phase. Apparent difference mainly observed in the second rapid decline phase, which directly linked to the filling status of the rivet cavity. By observing the filling status of the rivet cavity in **Fig. 33** and the starting time of the second rapid decline of the t_1 in **Fig. 35**(a), it could be found that the t_1 rapidly decreased again when the rivet cavity was nearly filled up. This is because the rivet itself as well the materials filled inside the rivet cavity applied a large pressure on the bottom sheet. The rivet cavity in the Riv-Bonding process was filled up at an earlier time, which led to the earlier occurrence of the second rapidly declined of the t_1. As a result, the final value of the t_1 in the Riv-Bonded joint (0.64mm) was smaller than the final value in the SPR process (0.87mm).

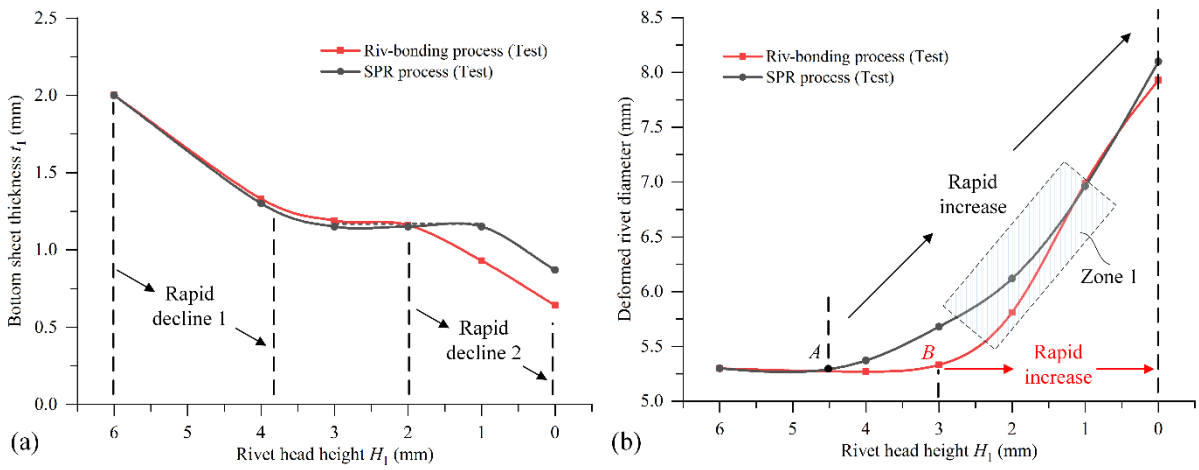

Fig. 35 Changing curves of (a) the remaining bottom sheet thickness at the joint centre t_1 and (b) the deformed rivet shank diameter

Fig. 35(b) shows the changing curves of the deformed rivet shank diameter for the two processes. During the SPR process, the rivet shank underwent very limited deformation at the early stage until the rivet head height H_1 became smaller than 4.5mm (point *A*). With further decrease of the H_1 from 4.5mm to 0mm, the deformed rivet shank diameter rapidly increased from the initial value 5.3mm to 8.10mm. While during the Riv-Bonding process, the rapid increase of the deformed rivet shank diameter started at a much later time when the H_1 reduced to around 3.0mm (point *B*). This delay directly linked to the smaller riveting force at the early stage of the Riv-Bonding process, as shown in **Fig. 34**. Meanwhile, the longer contact length between the rivet shank and the top sheet (blue dash line in **Fig. 33**(a-1)) also partially caused this delayed rivet shank deformation. Then, the increasing speed of the rivet shank diameter during the Riv-Bonding process surpassed that during the SPR process in Zone 1, and the rivet shank diameter reached to almost same value in

the two processes ($H_1 \approx$ 1.0mm). This phenomenon could be also explained by the different filling status of the rivet cavity. The rivet cavity in the Riv-Bonding process was filled up at an earlier time ($H_1 \approx$ 2.5mm) than in the SPR process ($H_1 \approx$ 0.5mm). It has been proved by Liu et al. (2019) that the materials filled inside the rivet cavity could facilitate the rivet shank flare. With further decrease of the H_1, the rivet cavity in the SPR process was also fully filled, and the rivet shank diameter increased at a slightly higher speed than that in the Riv-Bonding process. The final rivet shank diameter of the Riv-Bonded joint was slightly smaller compared with that of the SPR joint. Therefore, the adhesive layer could impose a negative effect on the rivet shank deformation, which has an adverse influence on the interlock formation.

4.2 Influences on the joint quality

As discussed above, the adhesive layer imposed a significant influence on the riveting process. As a result, the joint quality was also affected. The effects can be quantitatively assessed by the measured key dimensions, including the interlock (I_1), the rivet head height (H_1), the diameters of the interlock inner (D_1) and outer (D_2) boundaries, the remaining bottom sheet thickness at the joint centre (t_1) and under the rivet tip (t_2). **Fig. 36** shows the comparison of these values between the SPR joint 1-5 and the Riv-Bonded joint 2-5. It is obvious that the adhesive layer showed a negative impact on the interlock. The average interlock value for the Riv-bonded joint 2-5 is 95.9% of the values for the SPR joints 1-5. As discussed above, the adhesive layer led to a larger diameter of the inner interlock boundary (D_1) but a smaller diameter of the outer interlock boundary (D_2). Under the studied joint configuration, the D_1 increased by 0.04mm but the D_2 decreased by 0.05mm for the Riv-Bonded joint 2-5. This is the direct reason for the slightly smaller interlock in the Riv-Bonded joint. The measured rivet head height (H_1) is the same for the two types of joints. The adhesive layer also demonstrated a negative effect on the remaining bottom sheet thickness at the two critical regions. Both of the bottom sheet thickness at the joint centre (t_1) and under the rivet tip (t_2) demonstrated a decreasing trend once the adhesive was involved. The t_1 and t_2 in the Riv-Bonded joints 2-5 are 67.0% and 96.4% of the values for the SPR joint 1-5 respectively. This is mainly associated to the filling status of the rivet cavity and the changes of the rivet shank deformation behaviour in the Riv-Bonding process. Meanwhile, these quality differences of the mechanical connection in the Riv-Bonded joints might also attributed to the slightly increased total stack thickness caused by the remaining adhesive between the top and the bottom sheets.

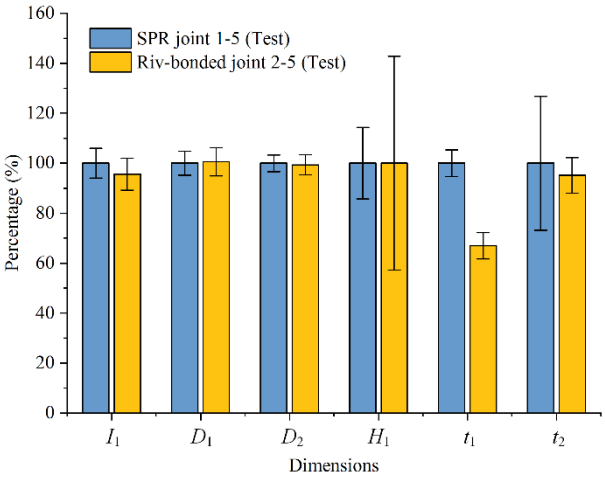

Fig. 36 Comparison of the measurements between the SPR joint 1-5 and the Riv-Bonded joint 2-5

5 Conclusions

A 2D simulation model of the Riv-Bonding process, suitable for industry applications, was developed in this study. Laboratory tests of the SPR process and the Riv-Bonding process were carried out to calibrate and verify the simulation model. The impacts of the adhesive layer on the riveting process and the joint quality were also experimentally investigated. The main conclusions are summarized below:

(1) The developed simulation model has the capability to predict the events happened during the Riv-Bonding process, and predicting the quality of the Riv-Bonded joints.

(2) The blank-holder strike has a significant influence on the Riv-Bonding process, and should be modelled properly in the simulation model.

(3) The Ostwald-de Waele power law was proved effective as the material constitutive of adhesives, and could be used to approximately predict the adhesive flow during the Riv-Bonding process.

(4) The adhesive layer imposed significant influences on the riveting process by affecting the load-displacement curve and the deformation behaviour of the rivet and the sheets.

(5) The adhesive layer led to a reduction in the interlock and the critical remaining bottom sheet thicknesses for the studied joint configuration.

This study for the first time developed a simulation model of the Riv-Bonding process suitable for industrial applications. It offers a new method to understand the Riv-Bonding process digitally and provides a foundation for future simulation model development, in terms of the quality and mechanical performance predictions under different joint configurations.

Acknowledgement

This work is funded by Jaguar Land Rover. The authors would like to thank Dr. Matthias Wissling, Paul Bartig and their team members from Tucker GmbH for their supports during the laboratory tests.

References

Abe, Y., Kato, T., Mori, K., 2008. Self-pierce riveting of three high strength steel and aluminium alloy sheets. Int. J. Mater. Form. 1, 1271–1274. https://doi.org/10.1007/s12289-008-0134-9

Alfano, M., Ambrogio, G., Crea, F., Filice, L., Furgiuele, F., 2011. Influence of Laser Surface Modification on Bonding Strength of Al/Mg Adhesive Joints. J. Adhes. Sci. Technol. 2511, 1261–1276. https://doi.org/10.1163/016942410X533381doi.org/10.1163/016942410X533381

Andersson, H.I., Aarseth, J.B., Braud, N., Dandapat, B.S., 1996. Flow of a power-law fluid film on an unsteady stretching surface. J. Nonnewton. Fluid Mech. 62, 1–8. https://doi.org/10.1016/0377-0257(95)01392-X

Anyfantis, K.N., Tsouvalis, N.G., 2012. A novel traction–separation law for the prediction of the mixed mode response of ductile adhesive joints. Int. J. Solids Struct. 49, 213–226. https://doi.org/10.1016/J.IJSOLSTR.2011.10.001

Ardakani, S.E., 2012. Entwicklung einer praxisnahen Methodik für die Simulation des Clinchklebeprozesses. PhD thesis. ISBN: 978-3-8440-1606-2. Universität Paderborn

Arenas Ã, J.M., Narbó, J.J., Alía, C., 2009. Optimum adhesive thickness in structural adhesives joints using statistical techniques based on Weibull distribution. Int. J. Adhes. Adhes. 30, 160–165. https://doi.org/10.1016/j.ijadhadh.2009.12.003

Balawender, T., Sadowski, T., Kneć, M., 2011. Technological problems and experimental investigation of hybrid: Clinched - Adhesively bonded joint. Arch. Metall. Mater. 56, 439–446. https://doi.org/10.2478/V10172-O11-0047-3

Baurova, N., Anoprienko, A., Romanova, Y., 2017. Providing dismountable rivet bonded joints through the use of hot-melt adhesives. MATEC Web Conf. 129, 01004. https://doi.org/10.1051/matecconf/201712901004

Carandente, M., Dashwood, R.J., Masters, I.G., Han, L., 2016. Improvements in numerical simulation of the SPR process using a thermo-mechanical finite element analysis. J. Mater. Process. Technol. 236, 148–161. https://doi.org/10.1016/J.JMATPROTEC.2016.05.001

Da Silva, L.F.M., Rodrigues, T.N.S.S., Figueiredo, M.A.V., de Moura, M.F.S.F., Chousal, J.A.G., 2006. Effect of

adhesive type and thickness on the lap shear strength. J. Adhes. 82, 1091–1115. https://doi.org/10.1080/00218460600948511

Di Franco, G., Zuccarello, B., 2014. Analysis and optimization of hybrid double lap aluminum-GFRP joints. Compos. Struct. 116, 682–693. https://doi.org/10.1016/J.COMPSTRUCT.2014.05.044

Esmaeili, F., Zehsaz, M., Chakherlou, T.N., Barzegar, S., 2015. Fatigue life estimation of double lap simple bolted and hybrid (bolted/bonded) joints using several multiaxial fatigue criteria. Mater. Des. 67, 583–595. https://doi.org/10.1016/J.MATDES.2014.11.003

Florian Hönsch, Josef Domitner, Christof Sommitsch, and B.G., 2020. Modeling the Failure Behavior of Self-Piercing Riveting Joints of 6xxx Aluminum Alloy. J. of Materi Eng and Perform. 29, 4888–4897 (2020). https://doi.org/10.1007/s11665-020-04894-8

Fratini, L., Ruisi, V.F., 2009. Self-piercing riveting for aluminium alloys-composites hybrid joints. Int. J. Adv. Manuf. Technol. 43, 61–66. https://doi.org/10.1007/s00170-008-1690-3

Fricke, H., Vallée, T., 2016. Numerical Modeling of Hybrid-bonded Joints. J. Adhes. 92:7–9, 652–664. https://doi.org/10.1080/00218464.2015.1100995org/10.1080/00218464.2015.1100995

Gerstmann, T., Awiszus, B., 2020. Hybrid joining: Numerical process development of flat-clinch-bonding. J. Mater. Process. Technol. 277, 116421. https://doi.org/10.1016/j.jmatprotec.2019.116421

Guo, Mingchao, and G.E.-T., 2020. Experimental Study on Static and Fatigue Performance of Self-Piercing Riveted Joints and Adhesively Bonded Self-Piercing Riveted Joints Connecting Steel and Aluminum Components. SAE Tech. Pap. https://doi.org/10.4271/2020-01-0177

Haque, R., Beynon, J.H., Durandet, Y., 2012. Characterisation of force–displacement curve in self-pierce riveting. Sci. Technol. Weld. Join. 17:6, 476–488. https://doi.org/10.1179/1362171812Y.0000000036

He, X., 2011. A review of finite element analysis of adhesively bonded joints. Int. J. Adhes. Adhes. 31, 248–264. https://doi.org/10.1016/J.IJADHADH.2011.01.006

He, X., Gu, F., Ball, A., 2012. Recent development in finite element analysis of self-piercing riveted joints. Int. J. Adv. Manuf. Technol. 58, 643–649. https://doi.org/10.1007/s00170-011-3414-3

He, X., Xing, B., Zeng, K., Gu, F., Ball, A., 2013. Numerical and experimental investigations of self-piercing riveting. Int. J. Adv. Manuf. Technol. 69, 715–721. https://doi.org/10.1007/s00170-013-5072-0

Hoang, N.H., Langseth, M., Porcaro, R., Hanssen, A.G., 2011. The effect of the riveting process and aging on the mechanical behaviour of an aluminium self-piercing riveted connection. Eur. J. Mech. A/Solids. 30, 619–630.

https://doi.org/10.1016/j.euromechsol.2011.02.006

Huang, L., Guo, H., Shi, Y., Huang, S., Su, X., 2017. Fatigue behavior and modeling of self-piercing riveted joints in aluminum alloy 6111. Int. J. Fatigue. 100, 274–284. https://doi.org/10.1016/j.ijfatigue.2017.03.006

Ishikawa, S., Aihara, H., 2017. Modelling of self-piercing riveting with ale, cel and sph based on abaqus/explicit. In COMPLAS XIV: proceedings of the XIV International Conference on Computational Plasticity: fundamentals and applications. 682-691. CIMNE

Jabbari, M., Bulatova, R., Hattel, J.H., Bahl, C.R.H., 2013. Quasi-steady state power law model for flow of (La 0·85 Sr 0·15) 0·9 MnO 3 ceramic slurry in tape casting. Mater. Sci. Technol. 29, 1080–1087. https://doi.org/10.1179/1743284713Y.0000000255

Li, D., Chrysanthou, A., Patel, I., Williams, G., 2017. Self-piercing riveting-a review. Int. J. Adv. Manuf. Technol. 92, 1777–1824. https://doi.org/10.1007/s00170-017-0156-x

Liu, Y., Li, H., Zhao, H., Liu, X., 2019. Effects of the die parameters on the self-piercing riveting process. Int. J. Adv. Manuf. Technol. 105, 1–16. https://doi.org/10.1007/s00170-019-04567-4

Liu, Y., Zhuang, W., 2019. Self-piercing riveted-bonded hybrid joining of carbon fibre reinforced polymers and aluminium alloy sheets. Thin-Walled Struct. 144, 106340. https://doi.org/10.1016/j.tws.2019.106340

Ma, Y., Lou, M., Li, Y., Lin, Z., 2018. Effect of rivet and die on self-piercing rivetability of AA6061-T6 and mild steel CR4 of different gauges. J. Mater. Process. Technol. 251, 282–294. https://doi.org/10.1016/J.JMATPROTEC.2017.08.020

Miyashita, Y., Jack Teow, Y.C., Karasawa, T., Aoyagi, N., Otsuka, Y., Mutoh, Y., 2011. Strength of adhesive aided SPR joint for AM50 magnesium alloy sheets. Procedia Eng. 10, 2532–2537. https://doi.org/10.1016/j.proeng.2011.04.417

Moraes, J.F.C., Jordon, J.B., Su, X., Barkey, M.E., Jiang, C., Ilieva, E., 2019. Effect of process deformation history on mechanical performance of AM60B to AA6082 self-pierce riveted joints. Eng. Fract. Mech. 209, 92–104. https://doi.org/10.1016/J.ENGFRACMECH.2018.12.020

Ozenc, M., Sekercioglu, T., 2014. Effect of surface pre-treatment and temperature on the adhesive strength of hybrid aluminum joints. Kov. Mater. Mater. 52, 1–10. https://doi.org/10.4149/km_2014_1_1

Porcaro, R., Hanssen, A.G., Langseth, M., Aalberg, A., 2006. Self-piercing riveting process: An experimental and numerical investigation. J. Mater. Process. Technol. 171, 10–20. https://doi.org/10.1016/j.jmatprotec.2005.05.048

Qu, S.G., Deng, W.J., 2008. Finite Element Simulation of the Self-Piercing Riveting Process. Vol. 4 Des. Manuf. 243–

249. https://doi.org/10.1115/IMECE2008-67017

Santos, T.F., Campilho, R.D.S.G., 2017. Numerical modelling of adhesively-bonded double-lap joints by the eXtended Finite Element Method. Finite Elem. Anal. Des. 133, 1–9. https://doi.org/10.1016/j.finel.2017.05.005

Sauer, R.A., 2016. A Survey of Computational Models for Adhesion. J. Adhes. 92, 81–120. https://doi.org/10.1080/00218464.2014.1003210

SikaPower ® -498, 2016. https://deu.sika.com/dms/getdocument.get/741b0a84-53dc-3677-981ce19cb4c0b6a3/SikaPower-498%20DE%2004-16.pdf

Sun, X., Stephens, E. V., Khaleel, M.A., 2007. Fatigue behaviors of self-piercing rivets joining similar and dissimilar sheet metals. Int. J. Fatigue. 29, 370–386. https://doi.org/10.1016/j.ijfatigue.2006.02.054

Van Hall, S.N., Findley, K.O., Freis, A.K., 2018. Improved self-pierce rivet performance through intentional decarburization. J. Mater. Process. Technol. 251, 350–359. https://doi.org/10.1016/J.JMATPROTEC.2017.08.018

Weber, G., Thommes, H., Gaul, H., Hahn, O., Rethmeier, M., 2011. Mechanical Properties of Weldbonded Joints of Advanced High Strength Steels. J. Adhes. Sci. Technol. 25, 2369–2389. https://doi.org/10.1163/016942411X580090

Weidong Dang, 2016. Finite element modelling of hybrid (spot welded/bonded) joints under service conditions. (Doctoral dissertation)

Zhang, X., He, X., Wei, W., Lu, J., Zeng, K., 2020. Fatigue characterization and crack propagation mechanism of self-piercing riveted joints in titanium plates. Int. J. Fatigue. 134, 105465. https://doi.org/10.1016/J.IJFATIGUE.2019.105465